Tropical Cyclones and Equatorial Waves in a Convection-Permitting Aquaplanet Simulation with Off-Equatorial SST Maximum

Rosimar Rios-Berrios[1], Christopher A Davis[2], and Jonathan Martinez[3]

[1]NCAR
[2]National Center for Atmospheric Research, P.O. Box 3000, 3450 Mitchell Lane, Boulder, Colorado 80307
[3]National Hurricane Center

May 25, 2023

Abstract

Tropical cyclogenesis can be influenced by convectively coupled equatorial waves; yet, existing datasets prevent a complete analysis of the multi-scale processes governing both tropical cyclones (TCs) and equatorial waves. This study introduces a convection-permitting aquaplanet simulation that can be used as a laboratory to study TCs, equatorial waves, and their interactions. The simulation was produced with the Model for Prediction Across Scales-Atmosphere (MPAS-A) using a variable resolution mesh with convection-permitting resolution (i.e., 3-km cell spacing) between 10oS–30oN. The underlying sea-surface temperature is given by a zonally symmetric profile with a peak at 10oN, which allows for the formation of TCs. A comparison between the simulation and satellite, reanalysis, and airborne dropsonde data is presented to determine the realism of the simulated phenomena. The simulation captures a realistic TC intensity distribution, including major hurricanes, but their lifetime maximum intensities may be limited by the stronger vertical wind shear in the simulation compared to the observed tropical Pacific region. The simulation also captures convectively coupled equatorial waves, including Kelvin waves and easterly waves. Despite the idealization of the aquaplanet setup, the simulated three-dimensional structure of both groups of waves is consistent with their observed structure as deduced from satellite and reanalysis data. Easterly waves, however, have peak rotation and meridional winds at a slightly higher altitude than in the reanalysis. Future studies may use this simulation to understand how convectively coupled equatorial waves influence the multi-scale processes leading to tropical cyclogenesis.

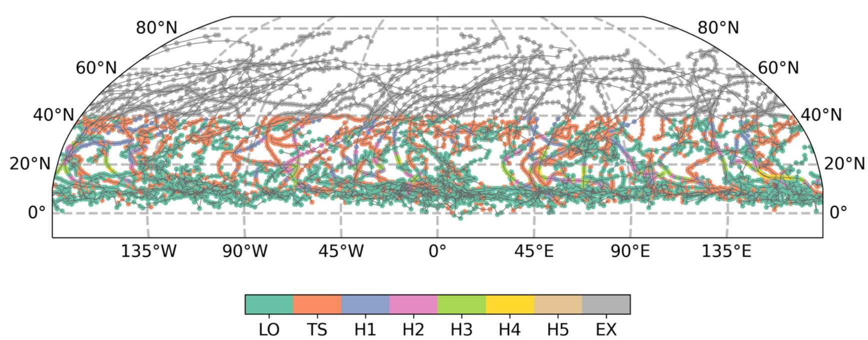

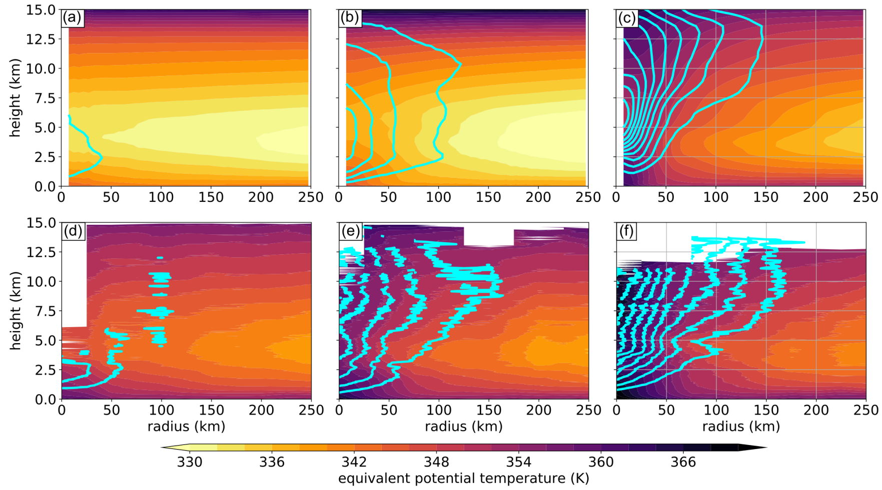

(a)
(b)
(c)
(d)
(e)
(f)
height (km)
radius (km)
equivalent potential temperature (K)
330
336
342
348
354
360
366

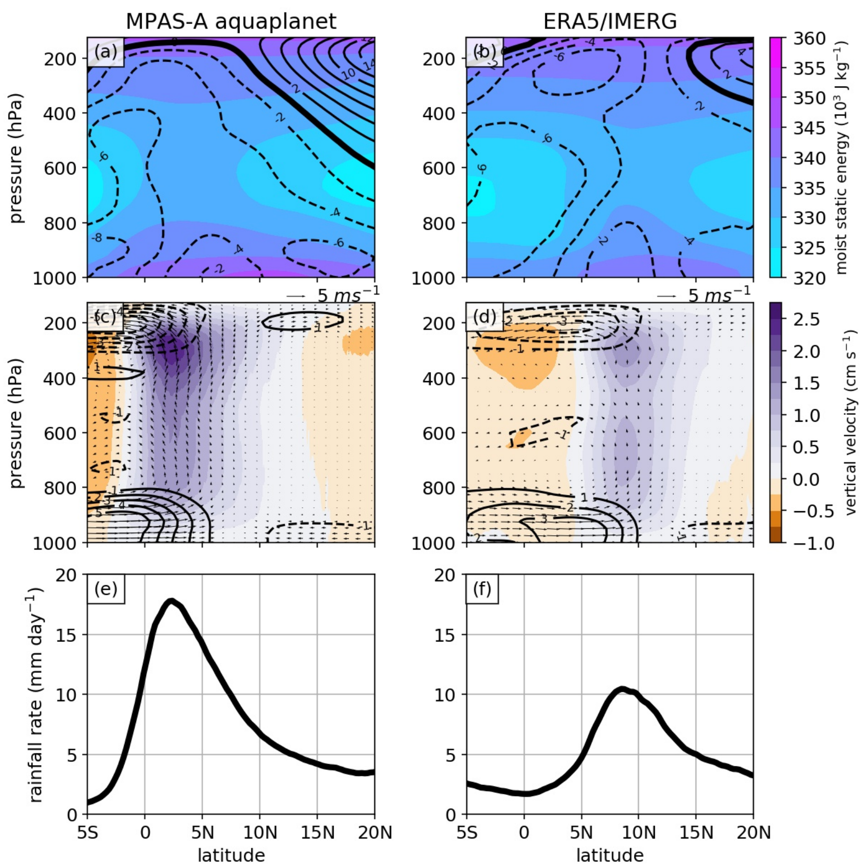

MPAS-A aquaplanet
ERA5/IMERG
(a)
(b)
(c)
(d)
(e)
(f)
pressure (hPa)
moist static energy (10^3 J kg^{-1})
vertical velocity (cm s^{-1})
5 ms^{-1}
rainfall rate (mm day^{-1})
latitude
5S
0
5N
10N
15N
20N

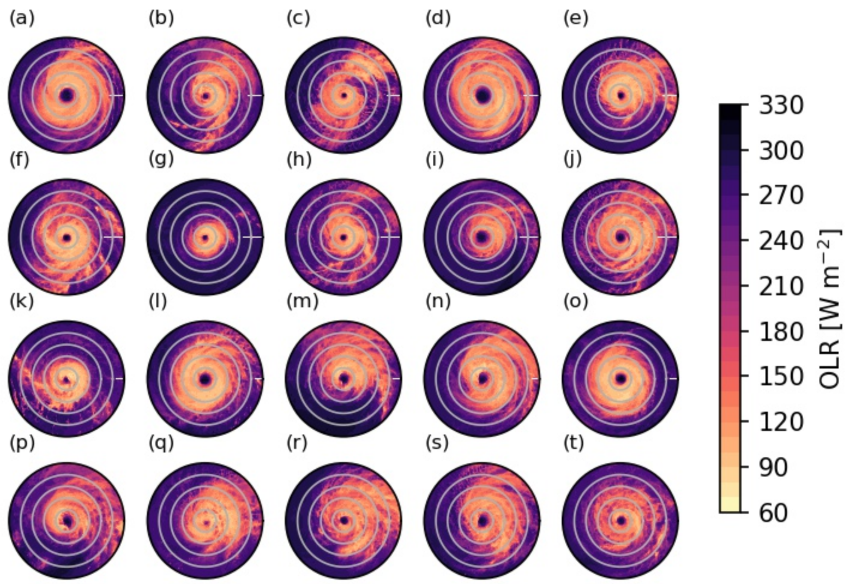

(a)
(b)
(c)
(d)
(e)
(f)
(g)
(h)
(i)
(j)
(k)
(l)
(m)
(n)
(o)
(p)
(q)
(r)
(s)
(t)
OLR [W m^{-2}]
330
300
270
240
210
180
150
120
90
60

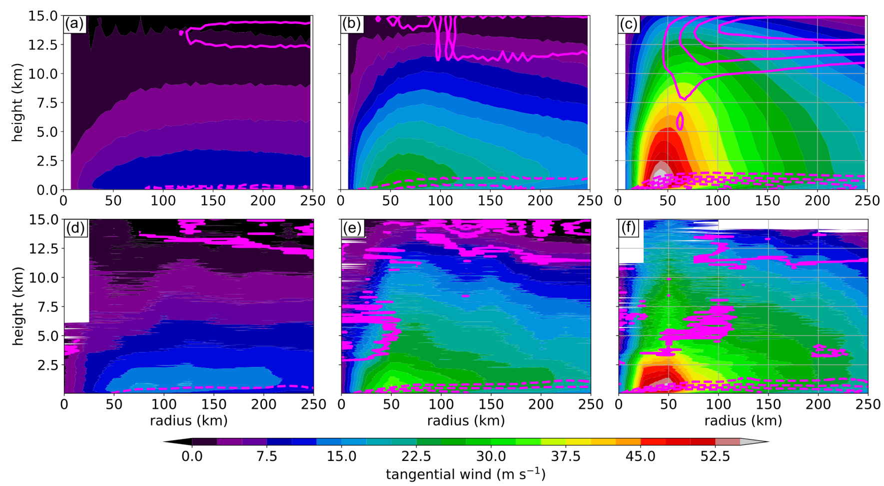

(a)
(b)
(c)
(d)
(e)
(f)
height (km)
radius (km)
0
50
100
150
200
250
15.0
12.5
10.0
7.5
5.0
2.5
0.0
tangential wind (m s^{-1})
37.5
45.0
52.5

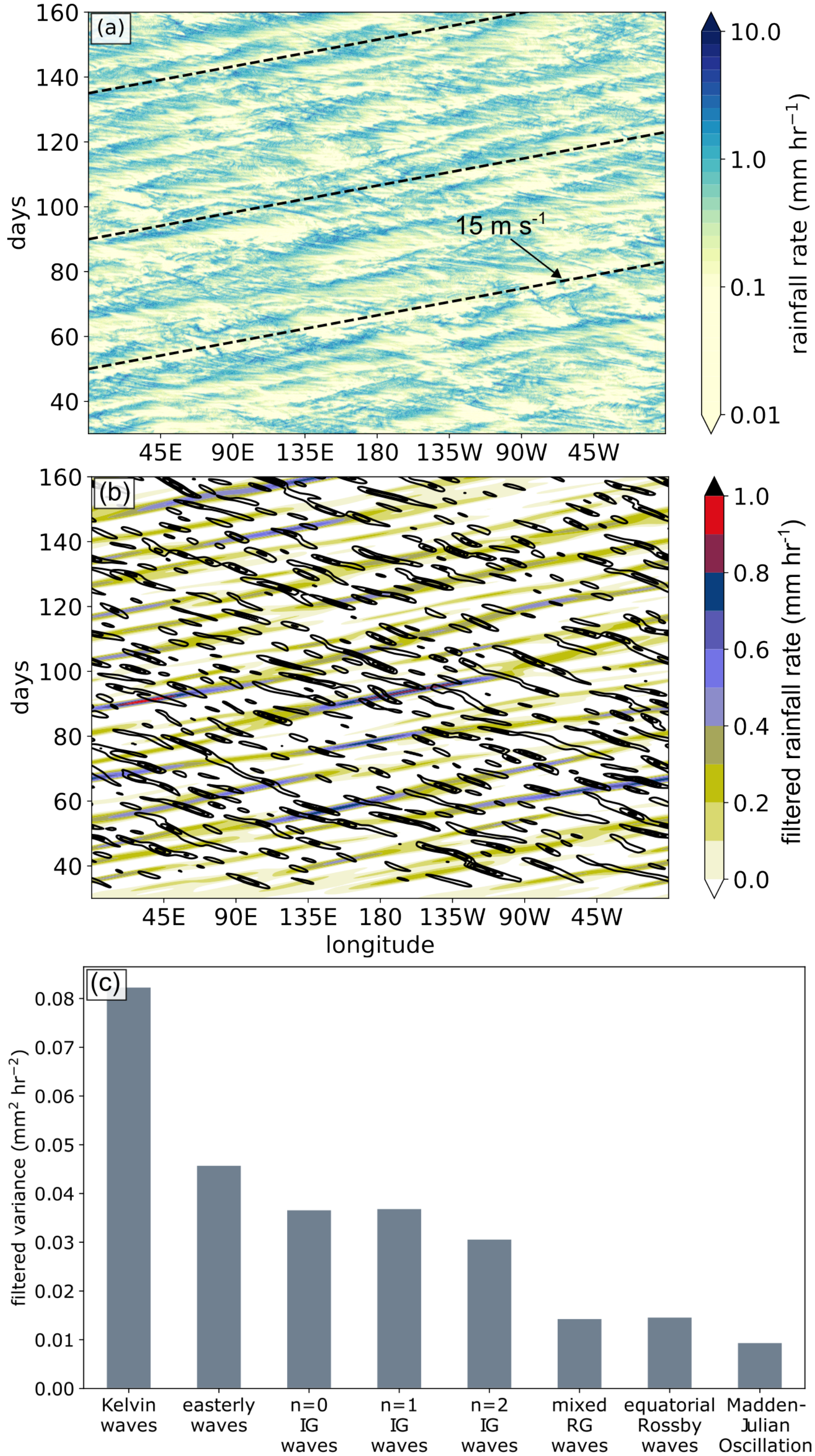

(a)
15 m s-1
days
rainfall rate (mm hr-1)
(b)
days
filtered rainfall rate (mm hr-1)
longitude
45E 90E 135E 180 135W 90W 45W
(c)
filtered variance (mm2 hr-2)
Kelvin waves
easterly waves
n=0 IG waves
n=1 IG waves
n=2 IG waves
mixed RG waves
equatorial Rossby waves
Madden-Julian Oscillation

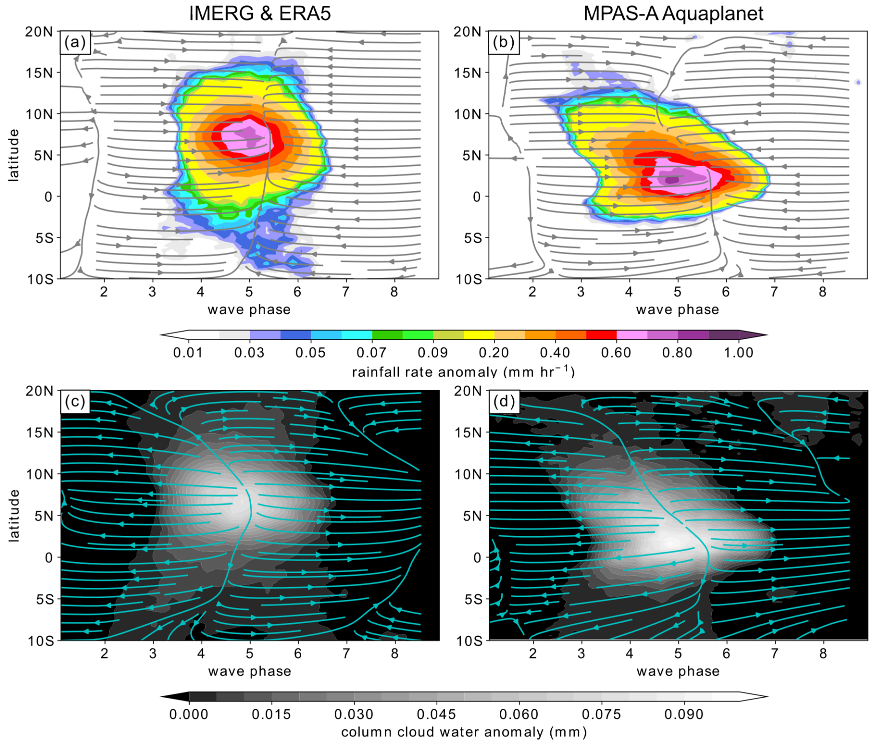
IMERG & ERA5
MPAS-A Aquaplanet
(a)
(b)
(c)
(d)
latitude
20N
15N
10N
5N
0
5S
10S
wave phase
2 3 4 5 6 7 8
0.01 0.03 0.05 0.07 0.09 0.20 0.40 0.60 0.80 1.00
rainfall rate anomaly (mm hr^{-1})
0.000 0.015 0.030 0.045 0.060 0.075 0.090
column cloud water anomaly (mm)

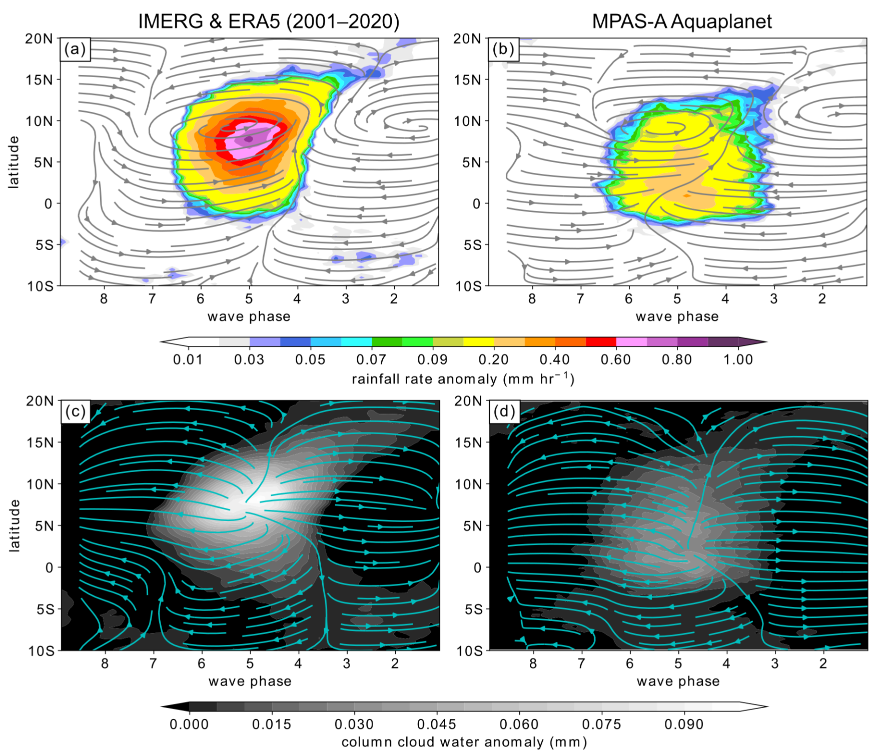
IMERG & ERA5 (2001–2020)
MPAS-A Aquaplanet
(a)
(b)
(c)
(d)
latitude
20N
15N
10N
5N
0
5S
10S
wave phase
8 7 6 5 4 3 2
0.01 0.03 0.05 0.07 0.09 0.20 0.40 0.60 0.80 1.00
rainfall rate anomaly (mm hr^{-1})
0.000 0.015 0.030 0.045 0.060 0.075 0.090
column cloud water anomaly (mm)

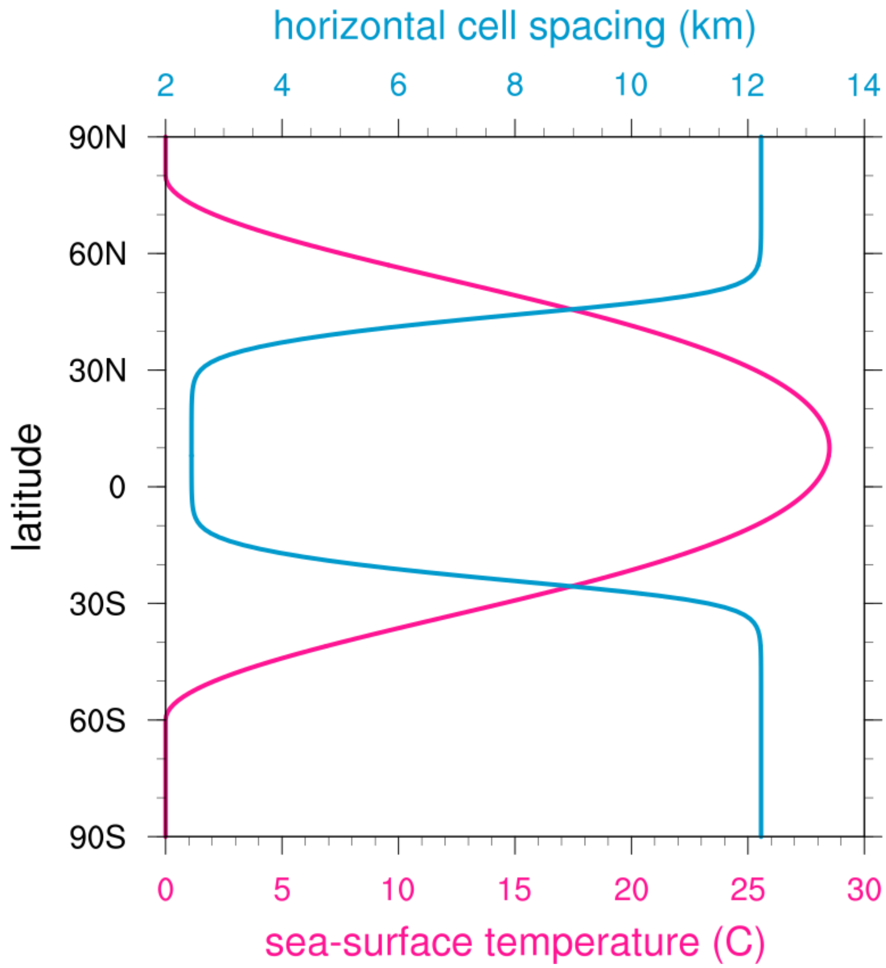
horizontal cell spacing (km)
2
4
6
8
10
12
14
90N
60N
30N
0
30S
60S
90S
latitude
0
5
10
15
20
25
30
sea-surface temperature (C)

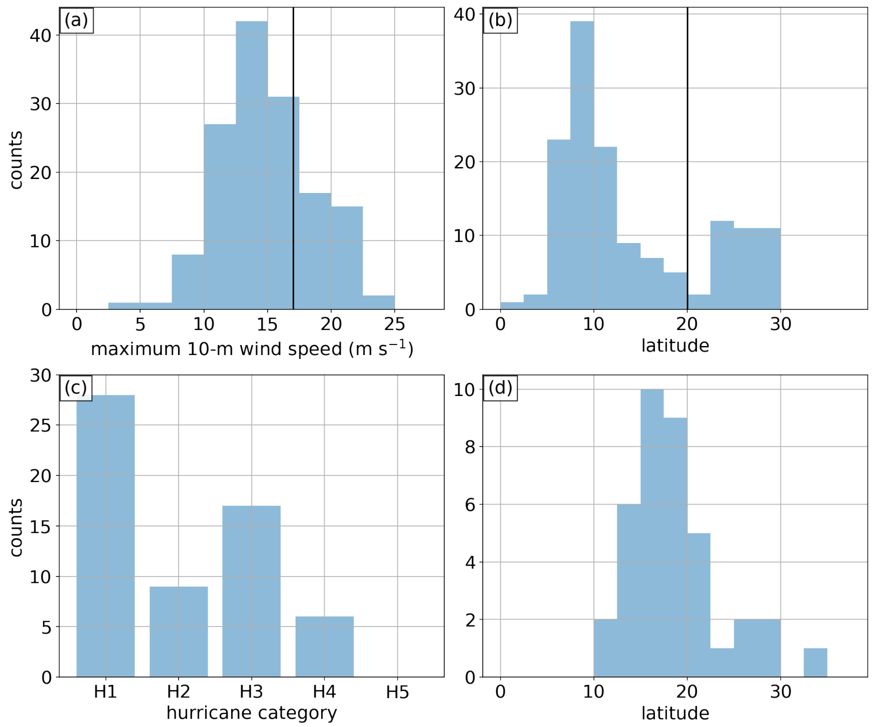

(a)
(b)
(c)
(d)
counts
maximum 10-m wind speed (m s^{-1})
latitude
hurricane category
H1
H2
H3
H4
H5

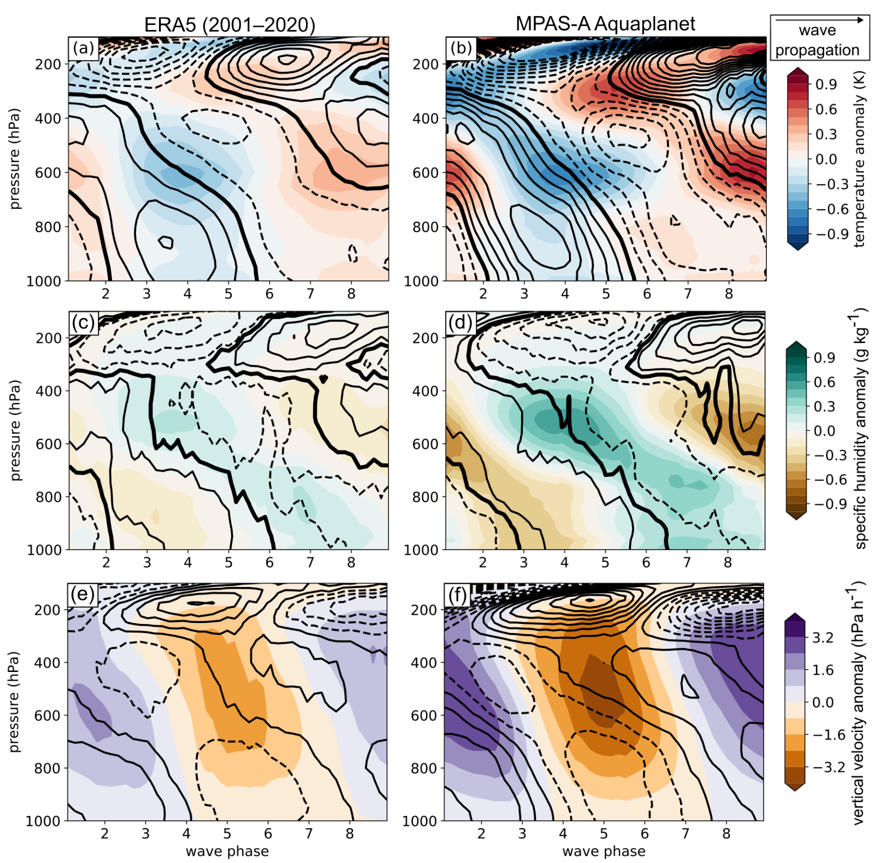

ERA5 (2001–2020)
MPAS-A Aquaplanet
wave propagation
(a)
(b)
(c)
(d)
(e)
(f)
pressure (hPa)
wave phase
temperature anomaly (K)
specific humidity anomaly (g kg^{-1})
vertical velocity anomaly (hPa h^{-1})

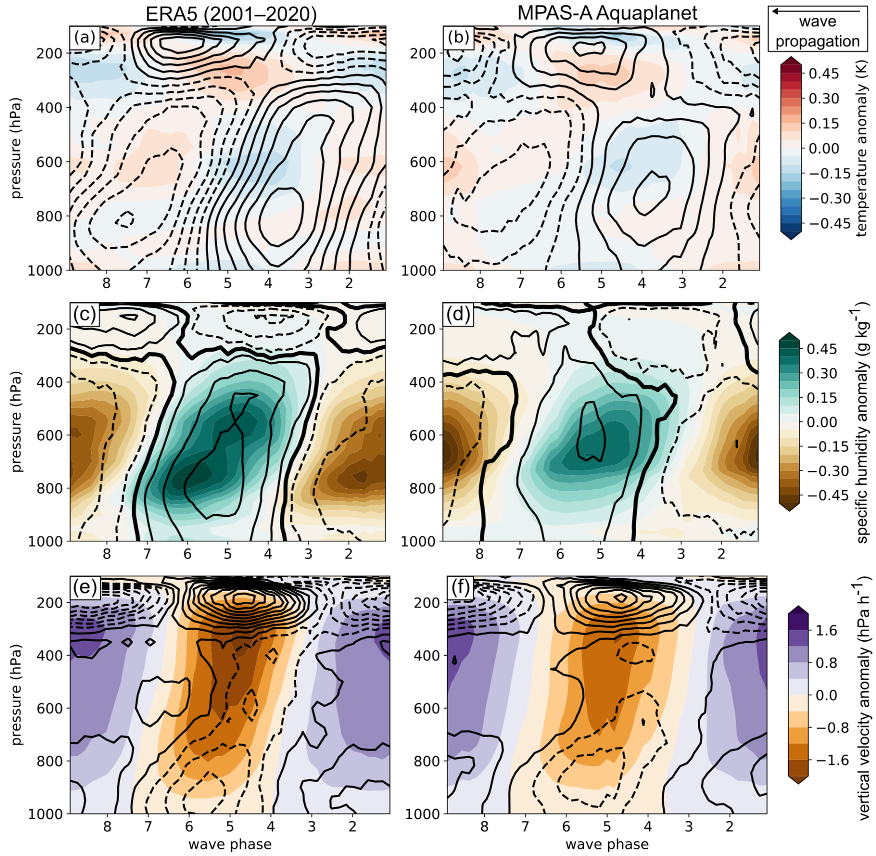

ERA5 (2001–2020)
MPAS-A Aquaplanet
wave propagation
(a)
(b)
(c)
(d)
(e)
(f)
pressure (hPa)
wave phase
temperature anomaly (K)
specific humidity anomaly (g kg^{-1})
vertical velocity anomaly (hPa h^{-1})

Tropical Cyclones and Equatorial Waves in a Convection-Permitting Aquaplanet Simulation with Off-Equatorial SST Maximum

Rosimar Rios-Berrios[1], Christopher A. Davis[1], and Jonathan Martinez[2]

[1]National Center for Atmospheric Research, Boulder, Colorado, USA
[2]Cooperative Institute for Research of the Atmosphere, Ft. Collins, Colorado, USA

Key Points:

- An aquaplanet simulation with convection-permitting resolution in the tropics is presented as a tool to study tropical weather phenomena
- The structure of tropical cyclones and equatorial waves is realistically captured despite the idealized configuration
- The simulation may be used for fundamental process-based studies of tropical cyclones, equatorial waves, and their interactions

Corresponding author: Rosimar Rios-Berrios, `rberrios@ucar.edu`

Abstract

Tropical cyclogenesis can be influenced by convectively coupled equatorial waves; yet, existing datasets prevent a complete analysis of the multi-scale processes governing both tropical cyclones (TCs) and equatorial waves. This study introduces a convection-permitting aquaplanet simulation that can be used as a laboratory to study TCs, equatorial waves, and their interactions. The simulation was produced with the Model for Prediction Across Scales-Atmosphere (MPAS-A) using a variable resolution mesh with convection-permitting resolution (i.e., 3-km cell spacing) between 10°S–30°N. The underlying sea-surface temperature is given by a zonally symmetric profile with a peak at 10°N, which allows for the formation of TCs. A comparison between the simulation and satellite, reanalysis, and airborne dropsonde data is presented to determine the realism of the simulated phenomena. The simulation captures a realistic TC intensity distribution, including major hurricanes, but their lifetime maximum intensities may be limited by the stronger vertical wind shear in the simulation compared to the observed tropical Pacific region. The simulation also captures convectively coupled equatorial waves, including Kelvin waves and easterly waves. Despite the idealization of the aquaplanet setup, the simulated three-dimensional structure of both groups of waves is consistent with their observed structure as deduced from satellite and reanalysis data. Easterly waves, however, have peak rotation and meridional winds at a slightly higher altitude than in the reanalysis. Future studies may use this simulation to understand how convectively coupled equatorial waves influence the multi-scale processes leading to tropical cyclogenesis.

Plain Language Summary

Despite many advancements in the science and prediction of tropical cyclones, scientists are still trying to explain the most important processes leading to the formation of tropical cyclones. An emerging area of focus is how atmospheric oscillations, known as Kelvin waves, may increase the likelihood that a disturbance (often times referred to as an easterly wave) may become a tropical cyclone. However, available atmospheric datasets are unable to capture all the fine details of tropical cyclones, disturbances, and Kelvin waves. To alleviate this challenge, this study presents a dataset based on a computer simulation of an Earth-like atmosphere except without continents or seasons. The simplicity of the simulation allows scientists to study the full life cycle of tropical cyclones—from their formation to their transformation into powerful hurricanes. The simulation also captures the full evolution and characteristics of Kelvin and easterly waves. Results of this study show that the simulated tropical cyclones, Kelvin waves, and easterly waves resemble those that happen in nature. Therefore, the simulation represents a useful dataset that future studies can exploit to advance our understanding of how tropical cyclones form and of how Kelvin waves affect the chances of tropical cyclone formation at a particular location and time.

1 Introduction

Aquaplanet simulations are idealized model representations of Earth's weather and climate. These simulations are typically configured as a water-covered sphere forced by a time-independent surface sea-temperature (SST) profile. The simple configuration allows a myriad of studies—from process-based studies of Earth's climate and weather to studies focused on model development and improvement (e.g., Hayashi & Sumi, 1986; Sumi, 1992; Hess et al., 1993; Held & Suarez, 1994; Williamson & Olson, 2003; Miura et al., 2005; Williamson, 2008; Medeiros & Stevens, 2011; Merlis et al., 2013, 2016; Chavas et al., 2017; Maher et al., 2019; Narenpitak et al., 2020; Medeiros et al., 2021). While most aquaplanet simulations are produced at a relatively coarse horizontal resolution [$\mathcal{O}$(100 km)] to allow for multi-year integration and multi-model comparison (e.g., Blackburn et al., 2013; Webb et al., 2017), recent studies have used aquaplanet simulations with high enough resolution [$\mathcal{O}$(1–10 km)] to capture mesoscale and convective-scale phenomena (Miura et al., 2005; Nasuno et al., 2007, 2008; Narenpitak et al., 2020; Rios-Berrios et al., 2022, 2023). This study builds on the growing number of relatively high-resolution aquaplanet simulations by introducing a convection-permitting aquaplanet simulation that captures realistic equatorial waves, tropical cyclones (TCs), and their interactions.

The aquaplanet simulation presented herein was designed to study multi-scale interactions leading to tropical cyclogenesis. It is widely accepted that TCs form in regions of favorable synoptic-scale conditions, including warm SSTs, weak vertical wind shear, and relatively moist troposphere (Gray, 1968). Recent studies suggest that those synoptic-scale conditions and the associated chances of tropical cyclogenesis can be modulated by the Madden-Julian Oscillation (Maloney & Hartmann, 2000, 2001; Hall et al., 2001; Kim et al., 2008; Klotzbach, 2010; Klotzbach & Oliver, 2014; Zhao et al., 2015; Klotzbach & Oliver, 2015) and convectively coupled equatorial Kelvin waves (Frank & Roundy, 2006; Bessafi & Wheeler, 2006; Schreck et al., 2010, 2011; Ventrice et al., 2012; Ventrice & Thorncroft, 2012; Schreck, 2015, 2016; Wu & Takahashi, 2017; Lawton et al., 2022). However, the literature offers conflicting explanations for the modulation of tropical cyclogenesis by equatorial Kelvin waves. Some studies argue that the modulation happens primarily through kinematic processes (e.g., reduced vertical wind shear, enhanced lower-tropospheric vorticity) (Bessafi & Wheeler, 2006; Ventrice & Thorncroft, 2012; Schreck, 2015), while other studies emphasize the role of moist convection and enhanced ascent associated with the waves (Frank & Roundy, 2006; Roundy, 2008; Wu & Takahashi, 2017; Lawton et al., 2022). These discrepancies motivated the design of an aquaplanet simulation with convection-permitting resolution in the tropics to capture the convective nature of both equatorial Kelvin waves and tropical cyclogenesis. While the aquaplanet framework may not capture the full complexities of the tropical atmosphere, this framework is a useful laboratory that isolates the most essential ingredients that are necessary for tropical oceanic convective phenomena.

Aquaplanet simulations have been extensively used to study many aspects of TCs (Merlis et al., 2013; Shi & Bretherton, 2014; Zhou et al., 2014; Ballinger et al., 2015; Reed & Chavas, 2015; Chavas et al., 2017; Merlis & Held, 2019; Narenpitak et al., 2020; Burnett et al., 2021; Stansfield & Reed, 2021; Vu et al., 2021; G. Zhang et al., 2021). Merlis and Held (2019) provided a review of different aquaplanet configurations historically used to study TC activity, including tropical cyclogenesis and TC motion. Those studies have shed new light on how and why TCs may change under a warmer climate. More recent studies have focused on specific aspects of TCs, such as the processes that distinguish developing from non-developing tropical disturbances (Narenpitak et al., 2020), the different TC rainfall distributions under varying SSTs (Stansfield & Reed, 2021), and the sensitivity of TC activity to the Coriolis force at the ITCZ location (Burnett et al., 2021).

Despite the frequent use of aquaplanet simulations to study TCs, there is limited evidence proving that the simulated TCs are consistent with observations. Reed and Chavas (2015) showed that aquaplanet simulations produced with the Community Atmosphere Model qualitatively captured the radial profile of azimuthally averaged TC tangential winds. Chavas et al. (2017) also showed that the same model captured a realistic pressure-wind relationship associated with TCs. However, those experiments did not fully capture the observed distribution of TC intensities owing to the absence of major hurricanes. Other aquaplanet experiments also have this deficiency, which most likely stems from their relatively coarse horizontal grid spacing (Merlis et al., 2013; Reed & Chavas, 2015; Chavas et al., 2017). Further evidence that the simulated TC structure and evolution are realistic is necessary to justify the aquaplanet configuration as a useful tool for fundamental studies of TCs.

Aquaplanet simulations have also been used to assess the representation of convectively coupled equatorial waves in global models (Nasuno et al., 2007; Frierson, 2007; Nasuno et al., 2008; Frierson et al., 2011; Andersen & Kuang, 2012; Blackburn et al., 2013;

Nakajima et al., 2013; Rios-Berrios et al., 2020; Rios-Berrios et al., 2022, 2023). This topic gathered special attention during the Aqua-Planet Experiment (Blackburn & Hoskins, 2013), an intercomparison of 14 aquaplanet simulations produced with different global models. An outcome of APE was the wide diversity of convectively coupled equatorial waves produced by the different models. In a follow-up study, Nakajima et al. (2013) compared the three-dimensional structure of the waves as represented by a subgroup of the APE participating models. Their comparison suggested that the diversity of equatorial waves and their structures could be attributed to differences in the cumulus parameterizations.

Rios-Berrios et al. (2020) introduced aquaplanet simulations using the Model for Prediction Across Scales-Atmosphere (MPAS-A), a model that was designed for seamless prediction of weather and climate. They demonstrated that the MPAS-A aquaplanet simulations captured convectively coupled equatorial waves, especially Kelvin waves, regardless of model resolution, physics packages, and vertical grid configuration. In follow-up studies, Rios-Berrios et al. (2022) and Rios-Berrios et al. (2023) described a variable resolution grid configuration with 3-km horizontal cell spacing in the tropics transitioning to 15-km cell spacing poleward of 40°N/S. Their comparison against MPAS-A aquaplanet simulations with different horizontal cell spacing showed that convection-permitting resolution in the tropics produced stronger and more realistic equatorial waves. However, easterly waves were not adequately represented in the MPAS-A aquaplanet experiments. They hypothesized that the SST profile (which was symmetric about the equator) was inadequate to capture the mean state and energetics that fuel easterly waves on Earth.

As computing resources increase, convection-permitting modeling experiments (including aquaplanet simulations) are becoming increasingly accessible. A recent model intercomparison showcased the ability of nine global models to produce 40-day hindcasts with convection-permitting resolution everywhere (Stevens et al., 2019). Those hindcasts improve the realism of modeled atmospheric phenomena in global models including TCs and equatorial waves (Stevens et al., 2019; Judt & Rios-Berrios, 2021; Jung & Knippertz, 2023); however, comparisons amongst the models reveal substantial intermodel spread, including different TC intensity distributions and different TC structures (Judt et al., 2021). Such spread implies that convection-permitting resolution alone will not solve many of the underlying deficiencies of global models. It is, therefore, important to evaluate if the computational expense of convection-permitting resolution yields valuable information that would not be otherwise available from coarser resolution (and hence computationally cheaper) models.

To this end, the main objectives of this study are:

1. to describe a novel MPAS-A aquaplanet simulation with an off-equatorial SST maximum and convection-permitting resolution in the tropics,
2. to investigate if the evolution and structure of the simulated TCs are consistent with observations, and
3. to determine if the simulated equatorial waves and their structure are adequately captured with an off-equatorial SST maximum.

This study is building on the work from Rios-Berrios et al. (2020), Rios-Berrios et al. (2022), and Rios-Berrios et al. (2023) by designing an experiment to investigate how TCs are represented in convection-permitting MPAS-A aquaplanet simulations. This experimental design may have implications for the representation of Kelvin waves and can enable future assessments of how Kelvin waves modify the cyclogenesis process in MPAS-A aquaplanet simulations. To this end, this manuscript is organized as follows. Section 2 describes the model configuration as well as the TC tracking and equatorial wave identification methods. Section 3 presents an analysis of the simulated tropical mean state,

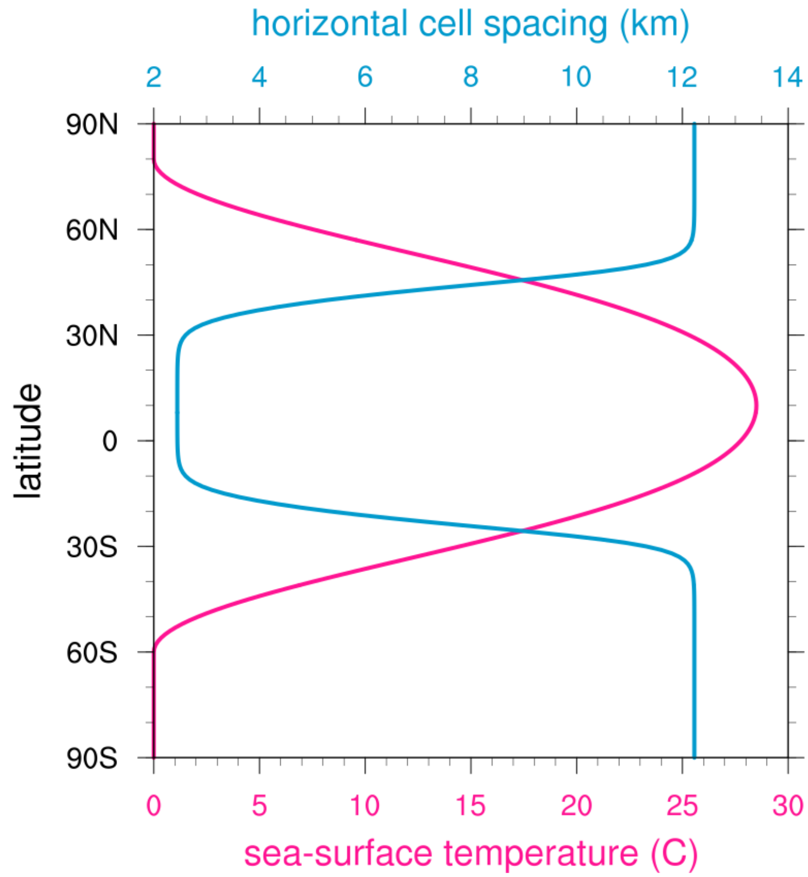

Figure 1. Approximate horizontal cell spacing (blue, top abscissa) and sea-surface temperature (pink, bottom abscissa) as a function of latitude.

TC statistics and structure, and equatorial waves structure. Lastly, Section 4 presents a summary and conclusions of this study.

2 Methods

2.1 Experimental setup

We produced an aquaplanet simulation using the Model for Prediction Across Scales-Atmosphere (MPAS-A) (Skamarock et al., 2012). MPAS-A is a global, nonhydrostatic model that was specifically designed for seamless simulations of multi-scale weather phenomena. The model uses C-discretization on a Voronoi tessalation mesh, which allows for either globally uniform horizontal resolution or grid refinement to yield relatively high resolution in a sub-region within the global domain. We used the grid refinement capability to employ approximately 3-km cell spacing between 10°S–30°N (Fig. 1). The cell spacing gradually transitions to approximately 12.3 km poleward of 55°N and 30°S. This configuration yields convection-permitting resolution in the tropics, which is critical for capturing the convective-scale processes associated with both TCs and Kelvin waves.

The convection-permitting resolution is not centered at the equator because the underlying sea-surface temperature (SST) profile peaks at 10°N (Fig. 1). This profile was first used by Ballinger et al. (2015) to simulate tropical cyclogenesis in an aquaplanet configuration. The SST varies with latitude (ϕ) according to the following formulation:

$$\mathrm{SST}(\phi) = \begin{cases} \mathrm{SST}_0 \left\{ 1 - \frac{1}{2} \left[sin^2 \left(\frac{\phi-\phi_0}{140}\pi \right) + sin^4 \left(\frac{\phi-\phi_0}{140}\pi \right) \right] \right\}, & \phi_0 - 70^\circ < \phi < \phi_0 + 70^\circ \\ 0, & \text{elsewhere} \end{cases}$$

where SST_0 is the maximum SST (set as 28.5°C) and ϕ_0 is the latitude of SST_0 (set as 10°N). This hemispheric asymmetric SST profile supports an off-equator ITCZ, which is necessary for TC formation poleward of the ITCZ where the Coriolis force provides sufficient background vorticity (Merlis et al., 2013; Ballinger et al., 2015).

The aquaplanet configuration of MPAS-A follows closely after Rios-Berrios et al. (2020) and Rios-Berrios et al. (2022). The model domain is configured as a water-covered surface without land or sea-ice with a boundary condition given by the temporally fixed, zonally symmetric SST profile described above. There is a diurnal cycle, but there are no seasons owing to a perpetual equinoctial conditions (i.e., the maximum insolation is always at the equator). Together with the SST profile, these conditions resemble the mean September conditions. All aerosols are radiatively inactive, and the ozone distribution is given by a hemispheric symmetric distribution following the Aqua-Planet Experiment model intercomparison (Blackburn et al., 2013). Unlike most aquaplanet simulations discussed in Section 1, we use physics packages from the numerical weather prediction community because those packages are thoroughly tested for weather timescales, including TCs. These packages include: the WSM6 microphysics (Hong et al., 2006), YSU planetary boundary-layer scheme (Hong et al., 2004), RRTMG shortwave and longwave radiation (Iacono et al., 2008), and a scale-aware version of the new Tiedtke convection parameterization (W. Wang, 2022). The vertical grid consists of 70 levels stretching from 60-m vertical spacing near the surface to 500-m spacing between 10 km and the model top at 40 km. Other details of the simulation are the same as in Rios-Berrios et al. (2020) and Rios-Berrios et al. (2022).

A 160-day simulation was produced to simulate multiple tropical cyclogenesis events. The simulation is initialized from a quiescent atmosphere and a globally-uniform thermodynamic profile taken from the globally averaged sounding of the 120-km aquaplanet simulation of Rios-Berrios et al. (2020). Our results are not sensitive to the initial sounding because the model is integrated for a relatively long time and it achieves its own equilibrium. We examined the globally averaged precipitable water vapor and precipitation rate to quantify the equilibrium of the simulation used herein. Although not shown here, those quantities reached equilibrium shortly before 30 days. Only the last 130 days are used for analysis. Although this simulation period is much shorter than the multi-year period typically used with aquaplanet experiments, the simulation is long enough to yield over 100 TCs and a variety of equatorial waves, as it will be shown later. The computational expense (approximately 32,000 core-hours per simulated day, resulting in a total of 5.1 million core hours) and data volume (approximately 360 GB per simulated day, resulting in a total of 57.6 TB of model output) in NCAR's Cheyenne Supercomputing System (?, ?) prevent us from extending this simulation at this point.

2.2 TC tracking

We used a two-step method to identify and track TCs. The first step used the TRACK algorithm (K. I. Hodges, 1996, 1999; K. Hodges et al., 2017) to identify suitable TC candidates based on spectrally filtered vorticity every six hours. Details of the TRACK algorithm can be found in Hodges (1996) and Hodges (1999). TRACK has been extensively used to obtain TC tracks in global climate models and reanalysis datasets (e.g., Bengtsson, Hodges, & Esch, 2007; Bengtsson, Hodges, Esch, Keenlyside, et al., 2007; Strachan et al., 2013; K. Hodges et al., 2017; Roberts et al., 2020). For this step, we conservatively interpolated the MPAS-A output to an n256 Gaussian grid using the Climate Data Operators software (Jones, 1999; Schulzweida, 2022). TRACK then interpolated the output to a T63 spectral grid to retain wavenumbers 6–63. To identify TC candidates, TRACK checked that the spectrally filtered vorticity met the following conditions:

- a lower-tropospheric vorticity anomaly exceeding 10^{-5} s^{-1},
- the vorticity anomaly lasted for at least two days,
- the vorticity anomaly first appeared equatorward of 35°N,
- a warm core existed at one or more point in the lifetime of the vorticity anomaly, where the warm core was defined as a positive difference between vorticity at 850 hPa and 200 hPa,
- a vertically coherent vorticity tower existed at any point, as given by positive vorticity at 700, 600, 500, and 200 hPa above the 850-hPa anomaly.

TRACK retained the entire lifecycle of each TC candidate from the first appearance of a lower-tropospheric vorticity anomaly until it no longer met the TC criteria. TRACK also saved the location of nondeveloping TC candidates; that is, TC candidates that only met the first three conditions.

The second step refined the track and intensity output from TRACK based on the native, unstructured MPAS-A output. Each TRACK TC candidate position was used a first guess for a vorticity centroid algorithm following Nguyen et al. (2014). If the vorticity centroid algorithm converged to a location within 250-km from the original TRACK position, then the output from the vorticity centroid algorithm was designated as the final cyclone position. Otherwise, the TRACK position was retained and used as the final TC position. TC intensity was then diagnosed with the maximum 10-wind speed and minimum mean sea-level pressure within a 200-km radius from the cyclone position. Importantly, these wind and pressure metrics were obtained from the native (i.e., convection-permitting) six-hourly model output.

2.3 Cyclogenesis definition

Most of the TCs were first identified when they were low-pressure systems (i.e., a cyclonic circulation appeared in the lower troposphere, but no warm core or coherent vortex tower was evident yet). This allowed us to objectively define tropical cyclogenesis as the time when (1) the minimum sea-level pressure (after applying a 24-h running mean) decreased for at least 24 h, and/or (2) a closed isobar appeared around the TC candidate center. Either or both of these criteria must have been satisfied equatorward of 30°N. The first criterion characterizes tropical cyclogenesis as a *process* during which a warm core forms and the surface pressure decreases in response to the warm anomaly. The second criterion is a proxy for the presence of a closed surface circulation. Extensive testing and analysis led us to conclude that this objective definition is more robust than choosing a wind threshold (e.g., 17 m s^{-1}) or simply the first appearance point of a lower-tropospheric vorticity anomaly. If a cyclogenesis time was not identified with these criteria, the feature was considered a "false alarm" detection by TRACK and it was regarded as a non-developing TC.

2.4 Equatorial waves identification

Convectively coupled equatorial waves were identified using spatiotemporal filtering of rainfall rate. This method is successful at identifying equatorial waves in MPAS-A simulations (Rios-Berrios et al., 2020; Judt & Rios-Berrios, 2021; Rios-Berrios et al., 2022, 2023). For this method, we first conservatively interpolated the MPAS-A output onto a $0.25° \times 0.25°$ latitude-longitude grid. We then applied a fast Fourier transform to rainfall rates between 5°S–10°N. We only retained the desired time periods and wavenumbers for each wave, and then we applied an inverse fast Fourier transform to obtain wave filtered rainfall rates. Kelvin waves were defined as spanning time periods between 2.5–

20 days and wavenumbers 1–14, whereas easterly waves spanned time periods between 2.5–12 days and wavenumbers greater than six.

We employ a wave phase space when analyzing the composite structure of simulated Kelvin and easterly waves. This wave phase space was thoroughly described by Rios-Berrios et al. (2023); in short, the wave phase space consists of eight phases based on the normalized filtered rainfall anomaly and the normalized time tendency of the filtered rainfall anomaly. A convectively active wave phase (labeled phase 5 in this study) occurs when the filtered rainfall anomaly is positive and the time tendency of the filtered rainfall anomaly is zero. Likewise, a convectively suppressed phase (labeled phase 1 in this study) happens when the filtered rainfall anomaly is negative and the time tendency of the filtered rainfall anomaly is zero. All other phases represent the transition from convectively active to suppressed phase and vice versa. This phase space allows us to compare waves of different wavelengths, intensity, etc. in a common framework, while also accounting for the wide rainfall envelope associated with equatorial waves (Riley et al., 2011; Yasunaga & Mapes, 2012; van der Linden et al., 2016; Schlueter et al., 2019; Sakaeda et al., 2020). An important difference from Rios-Berrios et al. (2023) is that we removed grid points within a $1°\times1°$ box around any TC before we constructed the wave phase composites.

2.5 Observational datasets

To investigate if our aquaplanet simulation yield realistic TCs and equatorial waves, we compared those simulated phenomena against their observed counterparts. Observed TC structure was examined with the Tropical Cyclone Dropsondes (TC-DROPS) dataset (Zawislak et al., 2018), which contains dropsonde data from reconnaissance, surveillance, and research flights into and around TCs between 1996–2019. All dropsonde data are subject to the same quality control specifications and interpolated on a common vertical grid with 25-m resolution. We present TC-DROPS composites stratified by TC intensity. We constructed the composites by binning the dropsonde data into radius-height bins, and then taking the average of all data in each bin. This procedure was inspired by the dropsonde composites from Zhang et al. (2011; 2013). To maximize the signal-to-noise ratio, we used 25 km radial bins and required a minimum of 100 dropsondes per each radial bin at each height.

For the mean state and equatorial waves, we used satellite rainfall rates and reanalysis data as proxies for observations. We obtained rainfall rates from NASA's Integrated Multi-SatellitE Retrievals for GPM (IMERG; Huffman et al., 2019). IMERG contains rainfall rates estimated from a combination of radar and infrared satellite measurements taken by low-polar orbiting satellites. We used the "late" 30-minute product on a $0.1°\times0.1°$ latitude-longitude grid. As in Rios-Berrios et al. (2023), we used conservative interpolation to coarse grain the IMERG rainfall rates to six-hourly intervals on a $0.25°\times0.25°$ grid. This grid matches the resolution of the atmospheric fields, which we obtained from the ECMWF reanalysis 5th Generation (ERA5; Hersbach et al., 2020). The grid also matches the interpolated MPAS-A output used to analyze the equatorial waves.

Similar to the analysis of simulated waves, we identified the waves through spatiotemporal filtering of rainfall rates averaged between 0–15°N. Figure 2 shows the 2001–2020 summer (July-October) filtered rainfall variance associated with the two waves of interest (Kelvin and easterly wave). We focus on the region between 0–15°N and 150°E–100°W, which encompasses the peak variance associated with these waves in the Pacific Ocean. The spatiotemporal filtering considered all longitudes, but following identification we only retained the waves in the Pacific Ocean (where the aquaplanet is most similar to Earth). Lastly, we constructed wave composites using the same wave-phase-technique described above. We removed the annual and seasonal cycle from both IMERG and ERA5 datasets to compare *anomalies* between reanalysis and the aquaplanet simulation. We also removed

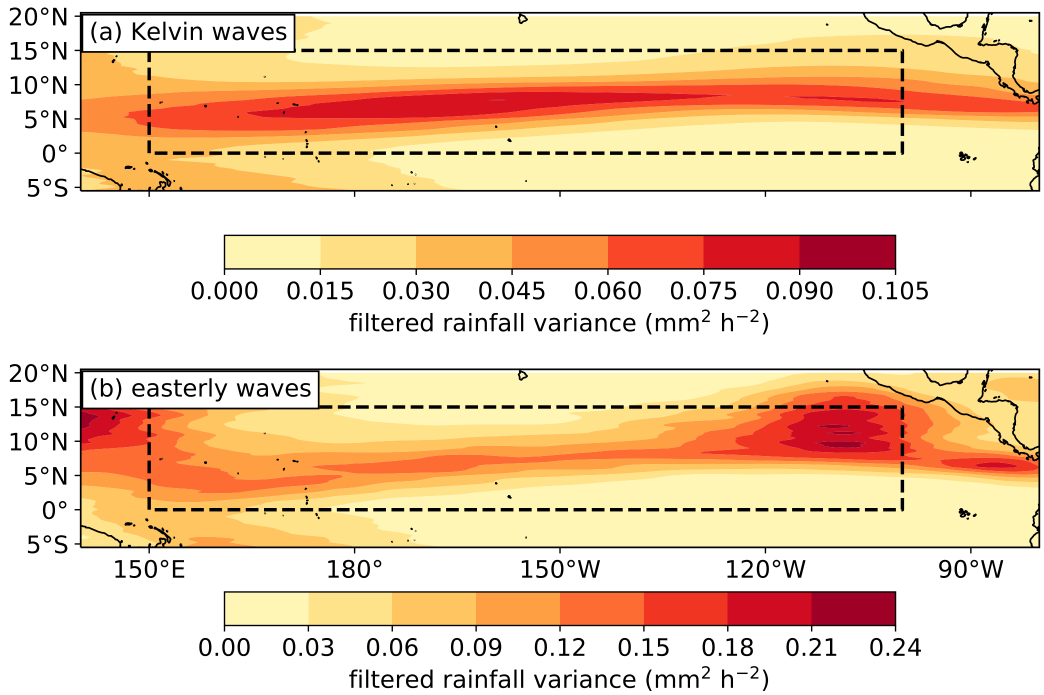

Figure 2. Variance of (a) Kelvin-filtered and (b) easterly-wave-filtered rainfall rates between 2001–2020. The box on each panel marks the domain considered for the wave composites.

grid points within a $1^\circ \times 1^\circ$ box around any TC, where the TC information was obtained from the International Best Track Archive for Climate Stewardship (IBTRACs; Knapp et al., 2010). Unlike Rios-Berrios et al. (2023) who considered all seasons, we only considered waves during summer (July-October) for consistency with the MPAS-A configuration used in this study.

3 Results

3.1 Mean state

The time mean, zonal mean state of the aquaplanet simulation is generally conducive for TC activity. Warm and moist conditions exist over the Northern Hemisphere tropics (between 0–10°N) as characterized by relatively high moist static energy (Fig. 3a). These conditions are accompanied by easterlies extending from the surface up to approximately 150 hPa, where the winds turn into westerlies (Fig. 3a). With weak westerlies aloft and easterlies near the surface, the tropics are associated with a mean westerly deep-layer vertical wind shear. Broad ascent and a rainfall peak also exist within the tropics in association with the rising branch of the Hadley cell (Figs. 3c,e). The ITCZ is off the equator in this simulation, although it is intriguing that the peak rainfall is located equatorward of the maximum SST. This is likely due to the competition between the fixed SST (which maximizes at 10°N) and the solar insolation (which maximizes at the equator).

Conditions become less conducive for TC activity poleward of 10°N in the aquaplanet simulation. The midtropospheric moist static energy minimum decreases by at least 10 K between 5°N and 20°N, which is indicative of relatively dry conditions (Fig. 3a). Rainfall rates also quickly decrease poleward of the ITCZ as indicated by daily averaged

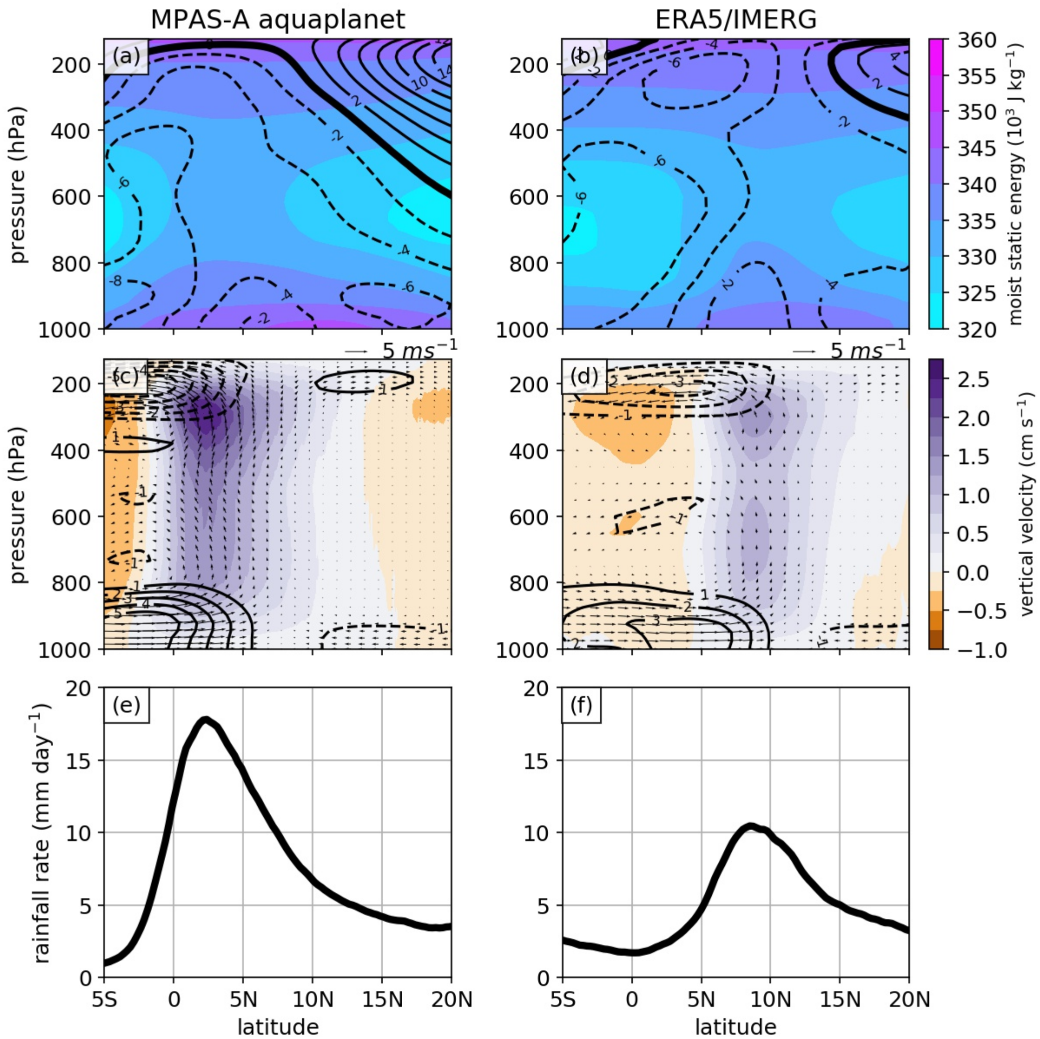

Figure 3. Time-averaged, zonally averaged analyses of (a,b) moist static energy (shading, every $5{\times}10^3$ J kg^{-1}) and zonal wind (contours, every 2 m s^{-1}), (c,d) vertical velocity (shading, every 0.25 cm s^{-1}) and meridional wind (contours, every 1 m s^{-1}), and (e,f) daily rainfall rates from (left) the MPAS-A aquaplanet simulation and (right) ERA5 and IMERG over the Pacific Ocean. The zero meridional wind contour is omitted in panels (c,d).

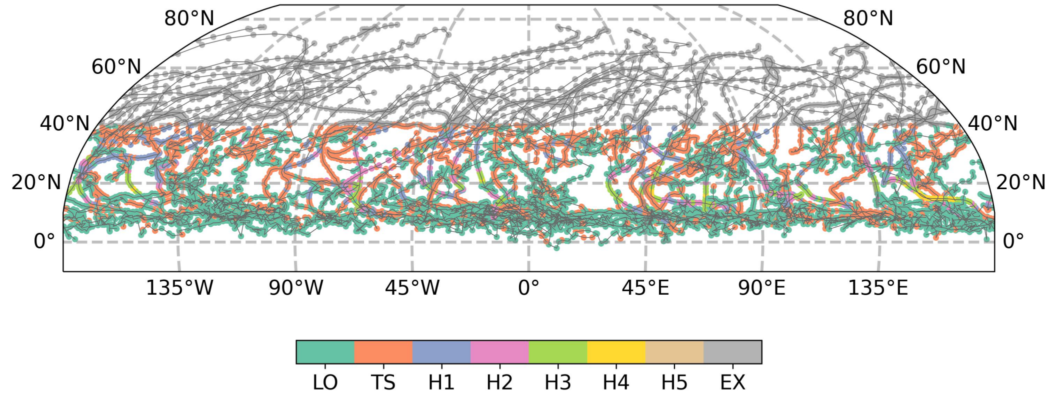

Figure 4. Global map of six-hourly TC positions. Colors indicate the intensity as estimated from the maximum 10-m wind speed within a 250-km radius from each cyclone center.

rainfall rates of approximately 5 mm day^{-1} at and poleward of 10°N (Fig. 3e). An upper-tropospheric westerly jet is also evident with its core above 12-km height and poleward of 20°N (Fig. 3a). The strengthening westerlies aloft bring strong deep-layer vertical wind shear exceeding 15 m s^{-1} by 20°N. The combination of dry conditions and relatively strong vertical wind shear are likely detrimental—on average—for TC formation and intensification.

To compare the simulated mean state against the observed mean state of the tropics, Figure 3 also shows the 2001–2020 time mean, zonal mean conditions over the Pacific Ocean (within the longitudinal domain marked in Fig. 2). A key difference is a general equatorward shift of the overturning circulation in the aquaplanet simulation. While deep easterlies and ascending moist air appear between 0–10°N in the aquaplanet simulation, those conditions appear between 5–15°N in the Pacific Ocean (Figs. 3a-d). Likewise, the ITCZ peaks between 0–5°N in the aquaplanet but closer to 10°N in the satellite-estimated rainfall. The Hadley circulation is also stronger in the MPAS-A aquaplanet simulation as evidenced by stronger lower-tropospheric southerlies (Figs. 3a,b), stronger vertical velocities (Figs. 3c,d), and heavier rainfall rates than in the reanalysis and satellite data (Figs. 3e,f). There is also stronger vertical wind shear in the aquaplanet simulation owing to the equatorward location of the upper-tropospheric jet in comparison to the conditions over the tropical Pacific.

3.2 Simulated TCs

Our MPAS-A aquaplanet simulation produces over a hundred unique TCs during the 130-day analysis period. Figure 4 shows their tracks and intensities. All TCs are detected in the Northern Hemisphere and at any longitude—this is a result of the prescribed zonally symmetric SST profile with a maximum at 10°. Most of the TCs first appear in the deep tropics (equatorward of 20°N), travel west-northwestward while also intensifying, and undergo extratropical transition once they reach the middle latitudes. When the SST profile peaks at the equator (Rios-Berrios et al., 2022), no TCs are detected. The need for an off-equatorial SST peak to trigger TCs is consistent with Merlis et al. (2013), who found that the number of TCs in an aquaplanet experiment is strongly tied to the latitudinal location of the ITCZ.

Using the objective definition of cyclogenesis, we find a wide range of TC intensities at the timing of cyclogenesis (Fig. 5a). Most TCs have maximum wind speeds weaker than 17 m s^{-1}, and no TC has yet reached hurricane strength. This result shows the ben-

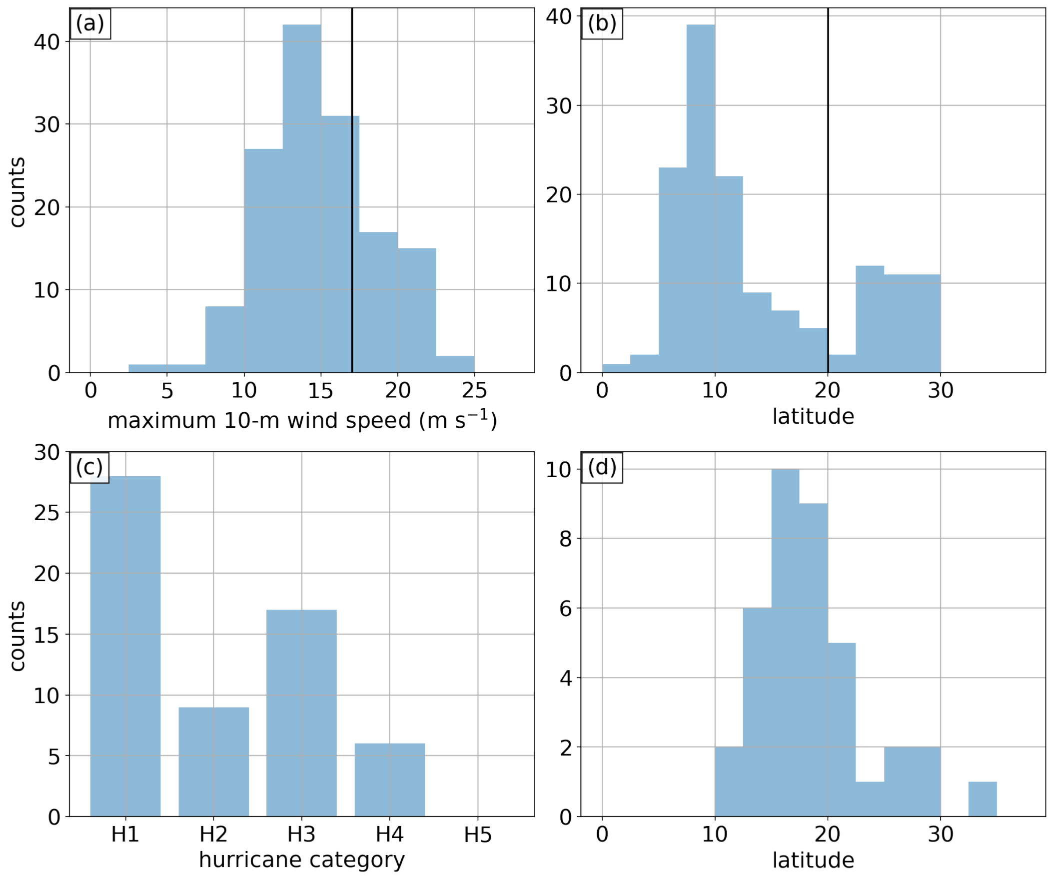

Figure 5. (a,b) Histograms of (a) maximum 10-m wind speed and (b) latitude at the time of cyclogenesis. Black lines mark 17 m s^{-1} on panel (a) and 20°N on panel (b). (c,d) Histograms of (c) hurricane intensity and (d) latitude at the time of lifetime maximum intensity only of TCs that reach hurricane strength.

efit of using a process-based objective method to define tropical cyclogenesis; using simply a maximum wind speed threshold could detect tropical cyclogenesis either too early or too late. Tropical cyclogenesis also happens in two primary regions in the aquaplanet experiment, as shown in the distribution of TC latitude at the time of cyclogenesis (Fig. 5b). The distribution shows two peaks: a primary peak equatorward of 20°N and a secondary peak between 25–35°N. The secondary peak is associated with midlatitude cyclones that undergo tropical transition (McTaggart-Cowan et al., 2008). For the rest of this study, we will focus only on the TCs that undergo cyclogenesis within the primary peak (i.e., equatorward of 20°N).

Of all TCs that form equatorward of 20° N, 61 become hurricanes (i.e., maximum 10-m wind exceeding 33 m s^{-1}). Figures 5c-d show distributions of intensity and latitude at the time when the hurricanes reach their lifetime maximum intensity (LMI). Most of the hurricanes are relatively weak; 29 TCs reach category-1 intensity and nine reach category 2. Importantly, the experiment also captures 23 major hurricanes as represented by 17 category-3 and six category-4 hurricanes. Although there are no category-5 hurricanes, the presence of major hurricanes creates a distribution of intensities closer to that of the real atmosphere. Furthermore, the absence of category 5 storms may reflect the overall less favorable conditions for hurricane development and intensification than

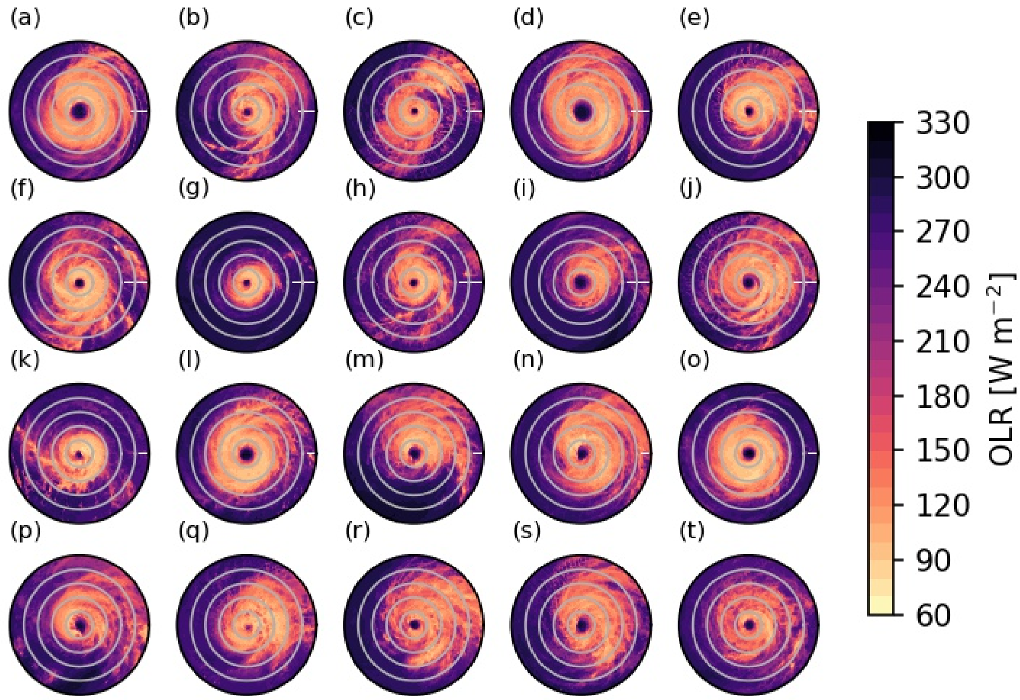

Figure 6. Storm-centered outgoing longwave radiation (shading, every 10 W m^{-2}) of 20 major hurricanes. Each snapshot extends 500-km radius from the TC center. Gray circles are plotted every 100 km.

in nature (e.g., Fig. 3). More than half of the simulated hurricanes reach their LMI between 10–20°N (Fig. 5d), whereas observed TCs reach their LMI between 18–25° latitude (Kossin et al., 2014; R. Wang & Wu, 2019). The slight equatorward shift of the LMI location in the aquaplanet further suggests that the less favorable conditions may be limiting the peak TC intensity in this simulation.

The simulated TC structure is consistent with observations. Figure 6 shows individual snapshots of outgoing longwave radiation at the time when 20 major hurricanes reached their LMI. These snapshots were obtained by linearly interpolating the native MPAS-A output into TC-relative cylindrical coordinates with 5-km radial spacing and 1° azimuthal bins. Although there is substantial variability amongst the major hurricanes, all of them exhibit the expected structure with a clear eye surrounded by the eyewall and rainbands. Some hurricanes have an eye that is about 200-km radius in diameter (e.g., Figs. 6a,d,i,l), while other hurricanes are much smaller and their cloud dense overcast barely covers 200-km in diameter (e.g., Figs. 6g,h,i). Furthermore, some hurricanes exhibit substantial convective asymmetry (Figs. 6b,e,i,m,p,r,s) while other hurricanes appear to be more "annular" or more symmetric (Figs. 6a,d,j,o). All these properties are characteristic of the variability amongst observed TCs, demonstrating that the aquaplanet simulation captures realistic TCs.

Further proof of the realism of the simulated TCs is their azimuthally averaged structure. Figures 7–8 show a comparison of the azimuthally averaged kinematic and thermodynamic structure against the dropsonde composites. The composites of simulated TCs consider only a single snapshot per TC at its LMI. During their tropical depression and tropical storm stage, both observed and simulated TCs are associated with a broad cyclonic vortex (Figs. 7a,d). The peak winds appear between 50–100 km radius from the

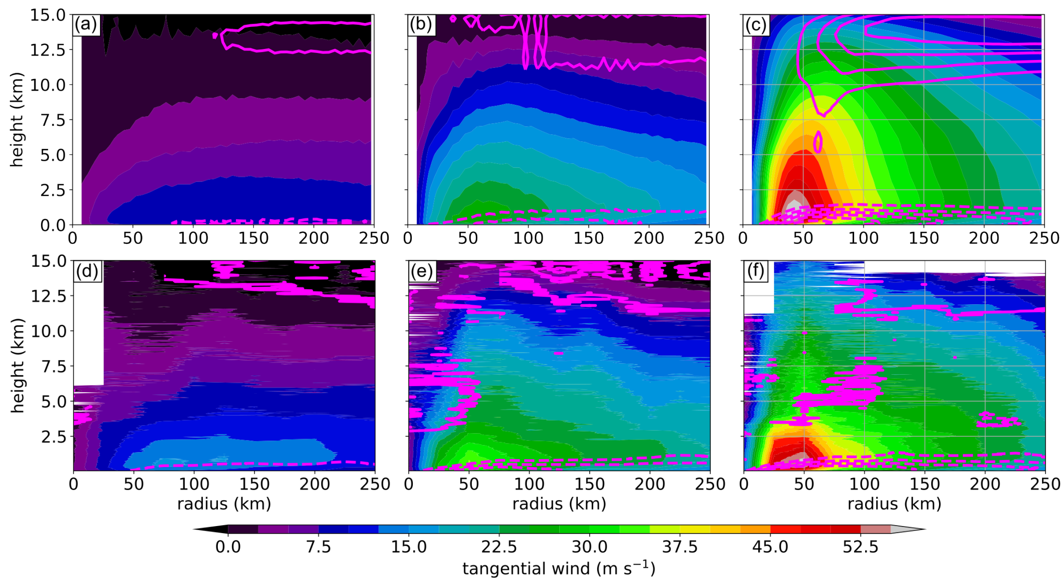

Figure 7. Height-radius composites of tangential wind (shading, every 2.5 m s^{-1}) and radial winds (pink contours, every 0.5 m s^{-1}) from (a)-(c) MPAS-A and (d)-(f) TC-DROPS. Panels show the composites for (a,d) tropical depressions and tropical storms, (b,e) category 1 and 2 hurricanes, and (c,f) major hurricanes. Solid contours represent positive radial wind (i.e., outflow) and dashed lines represent negative radial wind (i.e., inflow).

TC center, and a shallow layer of radial inflow exists in the lowest 1 km. A warm and moist reservoir exists near the surface as demonstrated by the equivalent potential temperature, while a warm temperature anomaly exists in the lower-to-middle troposphere (Figs. 8a,d). Intriguingly, the simulated equivalent potential temperature is at least 5 K lower in the aquaplanet simulation than in the TC-DROPS composites. This difference could be due to a drier equilibrium climate in the aquaplanet simulation, biases towards moist environments being sampled by the dropsonde data, or other factors.

As the TCs intensify, MPAS-A continues to realistically represent their structure. Notably, the cyclonic circulation strengthens, contracts in radius, and expands in height with increasing hurricane intensity (Figs. 7b,c,e,f). The radius of maximum azimuthally averaged tangential wind appears around 50–100 km for minor hurricanes (Figs. 7b,c) and inside 50-km radius for major hurricanes (Figs. 7e,f). The height of cyclonic winds increases with hurricane intensity, reaching up to at least 14-km height for major hurricanes. The boundary-layer inflow also deepens and strengthens together with strengthening outflow. The inner region of the simulated and observed hurricanes also warms and moistens as indicated by increasing equivalent potential temperature and a strengthening warm core (Figs. 8b,c,e,f).

For those hurricanes that reach category-3 intensity or higher, the simulated structure exhibits several noteworthy differences from the observed structure. The simulated hurricanes are associated with a stronger and deeper vortex than observed TCs as indicated by the tangential winds (Figs. 7c,f). The height of the warm core is also at a lower altitude than in the dropsondes composites—the warmest temperature anomaly appears around 6-km height in MPAS-A but around 10–12 km height in the dropsondes composites (Figs. 8c,f). Stern and Nolan (2012) argue that the primary warm core of TCs should be located around 4–8 km, although their results are based on idealized TC simulations. The differences in the warm core height presented herein could be due to the relatively

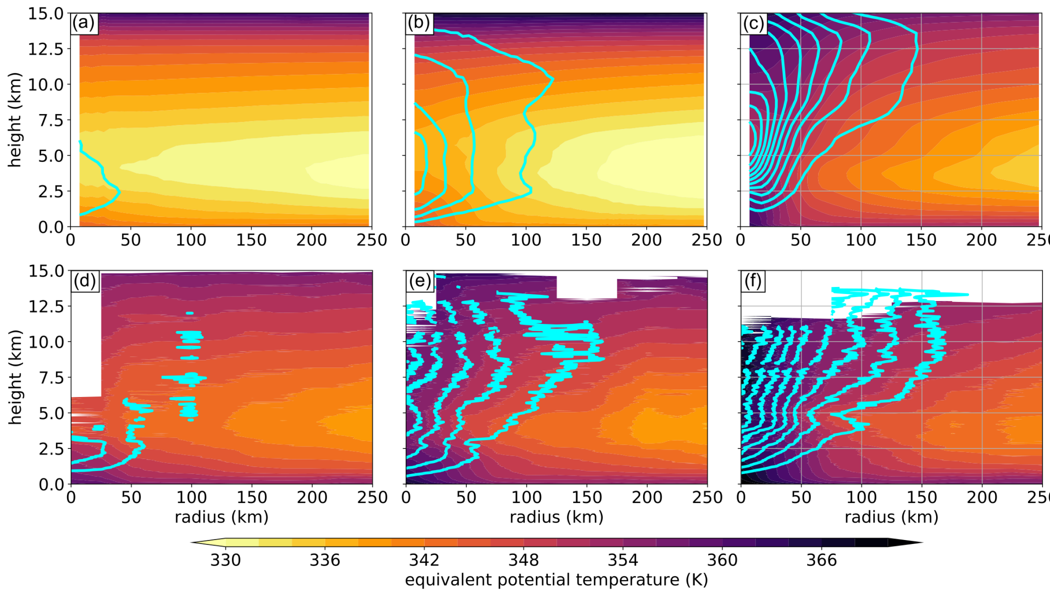

Figure 8. As in Fig. 7, except for equivalent potential temperature (shading, every 2 K) and temperature anomaly (contours, every 1 K) from the environment (approximated by temperature at 250-km radius).

small sample size of dropsondes above 3-km height and inside the radius of maximum winds.

Despite some of the differences noted between the observed and simulated major hurricanes, MPAS-A adequately captures the kinematic and thermodynamic structural features inherent to TCs in nature. Perhaps of equal importance, MPAS-A adequately captures the structural progression of TC circulations from the depression stage through major hurricane intensity.

3.3 Simulated equatorial waves

Despite the hemispheric asymmetric SST, our MPAS-A aquaplanet simulation captures tropical rainfall variability driven by convectively coupled equatorial waves (Fig. 9a). Rainfall rates averaged between 5°S–10°N show alternating periods of relatively light and heavy precipitation. Those alternating periods are primarily associated with eastward propagating disturbances that propagate at approximately 15 m s^{-1}, which is similar to the observed propagation speeds of Kelvin waves (Kiladis et al., 2009; Straub & Kiladis, 2003; Roundy, 2008). Applying a spatiotemporal filter to the rainfall rates confirms that the eastward propagating features can be described as Kelvin waves (Fig. 9b). Shorter-lived, smaller-scale disturbances are also evident within the broad rainfall anomalies (Fig. 9a). These disturbances propagate westward, and they are associated with easterly waves (Fig. 9b) and westward propagating inertio-gravity waves (not shown).

A quantitative analysis of the simulated equatorial waves is shown in Fig. 9c. This figure shows rainfall variance within different spatiotemporal domains corresponding to Kelvin waves, easterly waves, n=0,1,2 inertio-gravity waves, mixed Rossby-gravity waves, equatorial Rossby waves, and the Madden Julian Oscillation. The wavenumber and frequency limits for each group were deduced from Kiladis et al. (2009). Kelvin waves are the most active equatorial waves, which is consistent with other MPAS-A aquaplanet simulations (Rios-Berrios et al., 2020; Rios-Berrios et al., 2022, 2023). All other waves are associated with half or less than half of the rainfall variance associated with Kelvin waves. The second most active group corresponds to easterly waves, followed by inertio-gravity waves. Mixed Rossby-gravity waves and equatorial Rossby waves are not very active, as determined by their small rainfall variance.

Although there is some evidence of Madden-Julian Oscillation activity, its rainfall variance is the smallest amongst all waves considered and is nearly an order of magnitude smaller than the variance associated with Kelvin waves. We hypothesize that the infrequent occurrence of the Madden Julian Oscillation and Rossby-type waves is due to the zonally symmetric SST profile. Previous studies suggest that a zonal SST asymmetry—mimicking the western Pacific warm pool—is needed to trigger a Madden Julian Oscillation in the aquaplanet framework (Maloney & Shaman, 2008; MacDonald & Ming, 2022). Rossby-type waves may be present, although their signal may project onto different wavenumber-frequency space than its theoretical values due to doppler-shift effects (e.g., Nakajima et al., 2013; Das et al., 2016)

With evidence of equatorial waves in our simulations, we proceed to investigate if their structures are realistically represented by the aquaplanet simulation. For this purpose, we constructed wave-phase composites from MPAS-A and compared them against composites from ERA5 and IMERG, as described in Section 2. Figures 10–13 show the wave-phase composites of Kelvin and easterly waves. We focus on these two groups because of our intent to do a follow-up study on how the easterly waves are influenced by Kelvin waves during their transition to TCs. While Rios-Berrios et al. (2023) also examined wave-phase composites in their aquaplanet simulations, it is important to investigate if the simulated waves structures are affected by the different SST profile employed here. As a reminder, phase 5 corresponds to the convectively active phase of each wave. The abscissa is reversed for easterly waves because those waves propagate westward and the wave phases are chosen to represent east-west cross sections.

The MPAS-A aquaplanet experiment captures the key structural features of Kelvin waves (Figs. 10–11). These waves are associated with anomalous lower-tropospheric easterlies and upper-tropospheric westerlies to the east (i.e., wave phases 5–8) of their rainfall and cloudiness peaks (Figs. 10). Likewise, anomalous lower-tropospheric westerlies and upper-tropospheric easterlies appear to the west (i.e., wave phases 1–5) of the most active convection. Their vertical structure is characterized by alternating cool and warm anomalies during the convectively active phase (i.e., phase 5) (Fig. 11a,b). A "boomerang" type structure exists in temperature, where the temperature anomalies tilt westward with height up to approximately 200 hPa and then tilt eastward with height above 200 hPa. The zonal winds, water vapor, and divergence fields also exhibit a westward tilt with height from the surface up to approximately 200 hPa (Fig. 11c-f). Lower-tropospheric water vapor anomalies exist to the east of the peak convection, whereas mid-to-upper-tropospheric water vapor anomalies appear to the west of the rainfall peak (Fig. 11c,d). Lower-tropospheric convergence, deep ascent, and upper-tropospheric divergence exist during the convectively active phase of these waves (Fig. 11e,f). Consistent with their theoretical structure, rotation is very weak in these waves as represented by weak anomalies in the relative vorticity field (Fig. 11c,d). Yet, there is anomalous cyclonic vorticity co-located with anomalous westerlies and anomalous anticyclonic vorticity co-located with anomalous easterlies.

Several noteworthy differences are evident when comparing the simulated and observed Kelvin waves. Rainfall and cloud water anomalies extend poleward and westward from the rainfall peak in the aquaplanet simulation, but such pattern is less evident in IMERG. Rios-Berrios (2023) also noted those differences and attributed them to the frequent overlap between Kelvin waves and other westward propagating waves in the aquaplanet simulation. Another key difference is the magnitude of the anomalies associated with these waves. Peak temperature, water vapor, divergence/convergence, and vertical velocity anomalies are at least two times stronger in MPAS-A than in ERA5. This

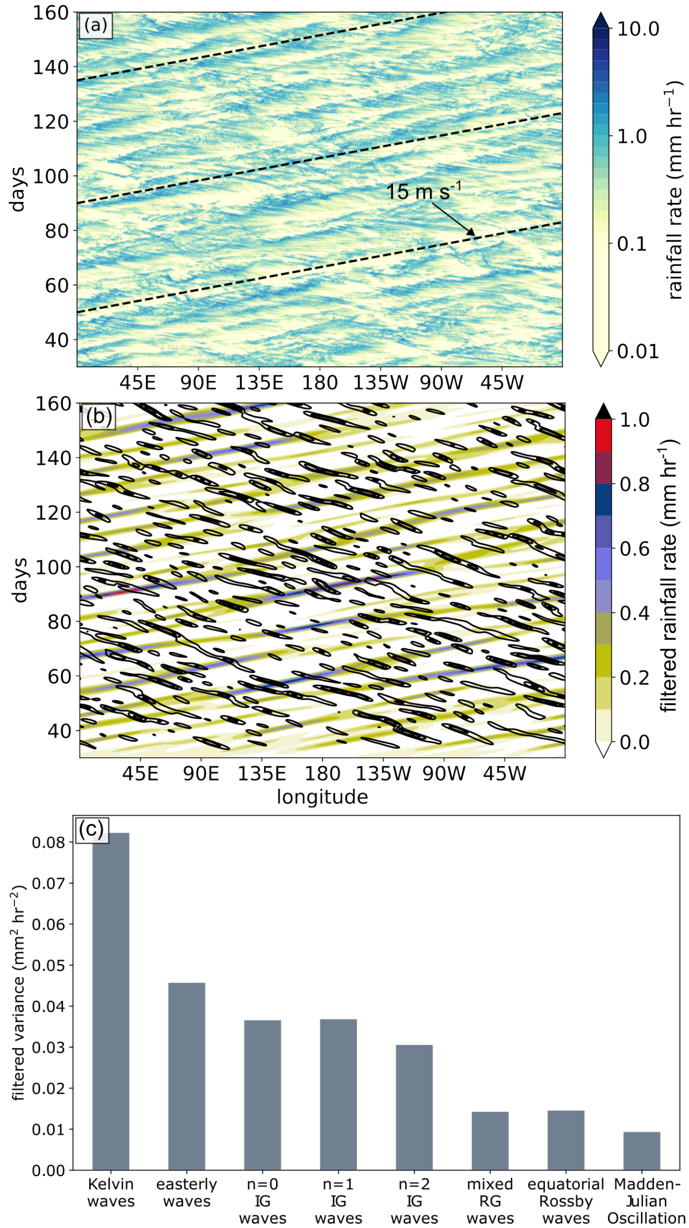

Figure 9. (a,b) Hövmoller diagram of (a) rainfall rates and (b) *filtered* rainfall rates averaged between 5°S–10°N from the MPAS-A aquaplanet experiment. In panel (a), the dashed lines illustrate the slopes of 15 m s−1 propagation speeds. Panel (b) shows Kelvin wave (shading, every 0.1 mm hr^{-1}) and easterly wave (contours, every 0.1 mm hr^{-1}) filtered rainfall rate anomalies. (c) Wave-filtered rainfall variance between 5°S–10°N.

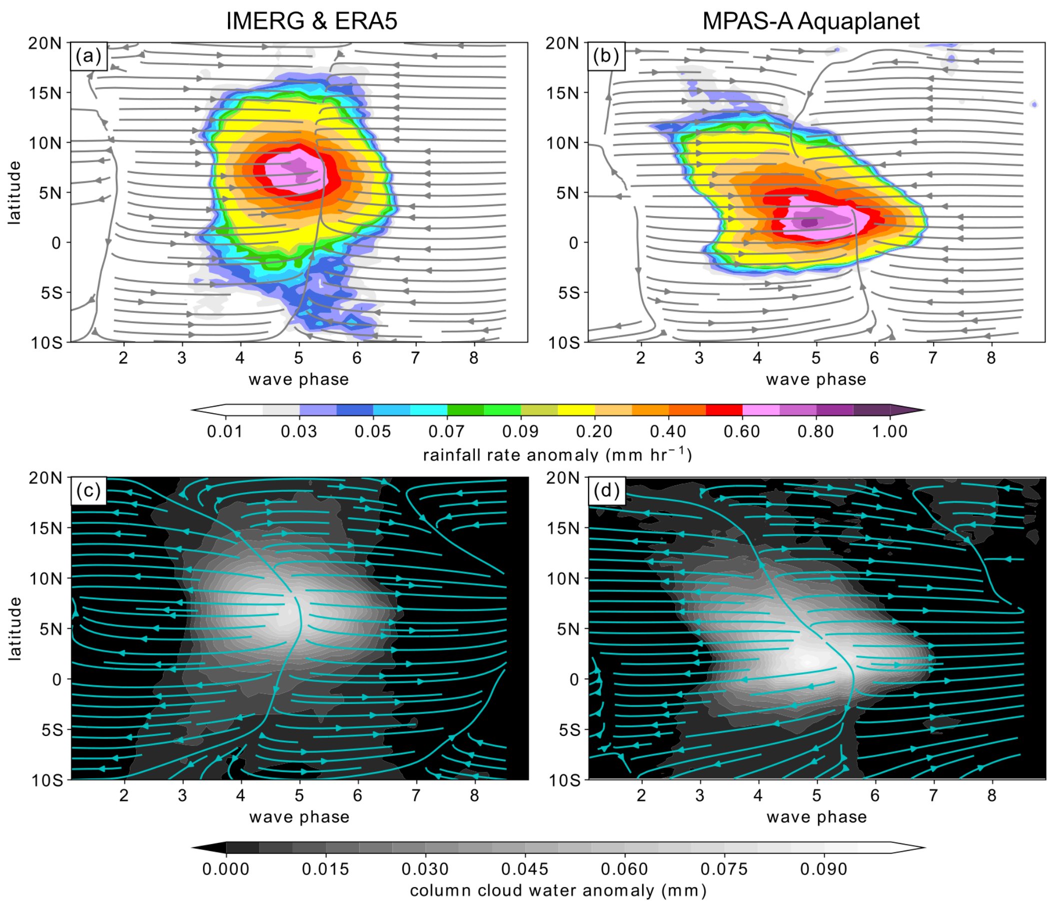

Figure 10. Latitude-wave phase composite anomalies associated with Kelvin waves in (a,c) ERA5/IMERG and (b,d) MPAS-A. Panels show (a,b) rainfall rate (shading) and 850-hPa anomalous winds, and (c,d) column integrated cloud condensate (shading) and 200-hPa anomalous winds.

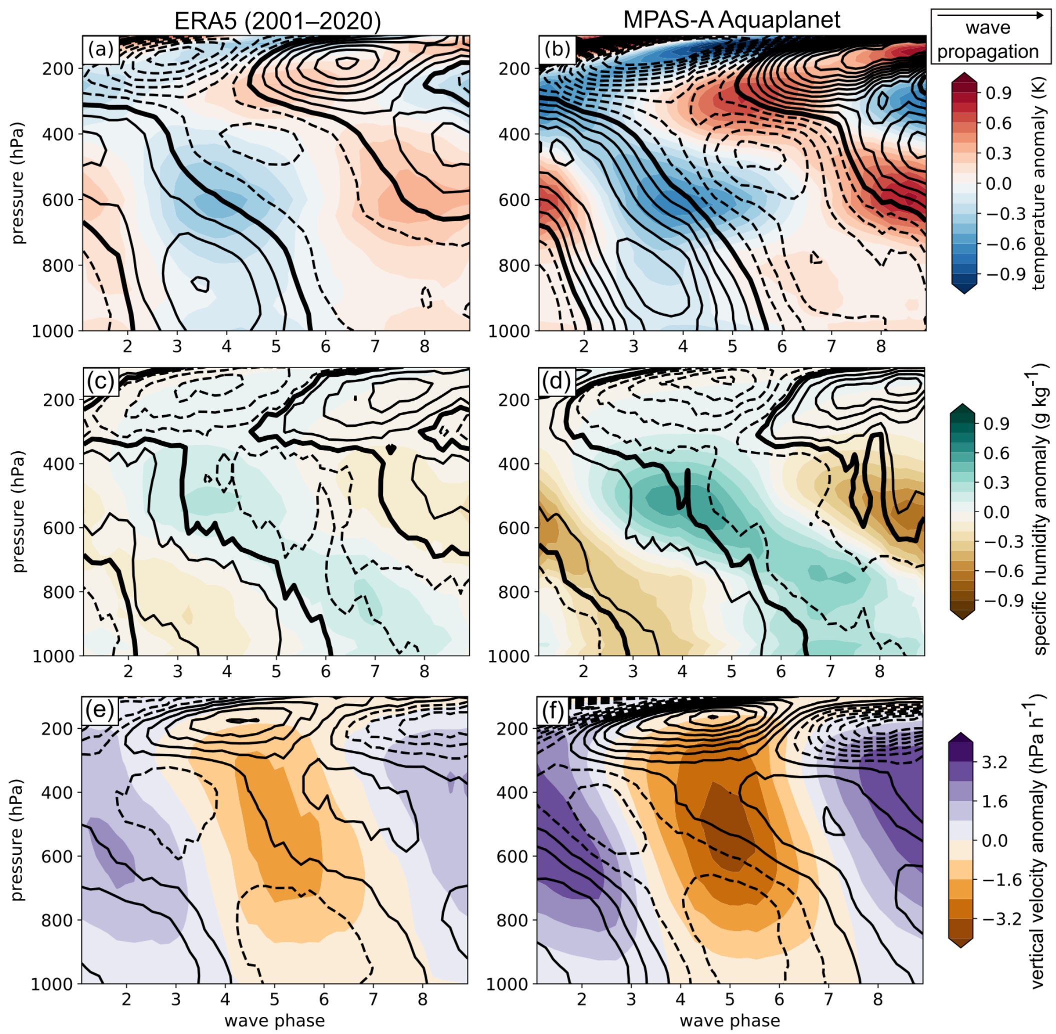

Figure 11. Pressure-wave phase composite anomalies associated with Kelvin waves in (a,c,e) ERA5/IMERG and (b,d,f) MPAS-A. Panels show (a-b) temperature (shading, every 0.1 K) and *zonal* wind (contours, every 0.5 m s^{-1}), (c-d) specific humidity (shading, every 0.1 g kg^{-1}) and relative vorticity (contours, every 0.1×10^{-5} s^{-1}), and (e-f) vertical velocity (shading, every 0.8 hPa h^{-1}) and divergence (contours, every 0.1×10^{-5}). In all panels, solid contours represent positive anomalies, dashed contours represent negative anomalies, and thick lines denote the zero contour.

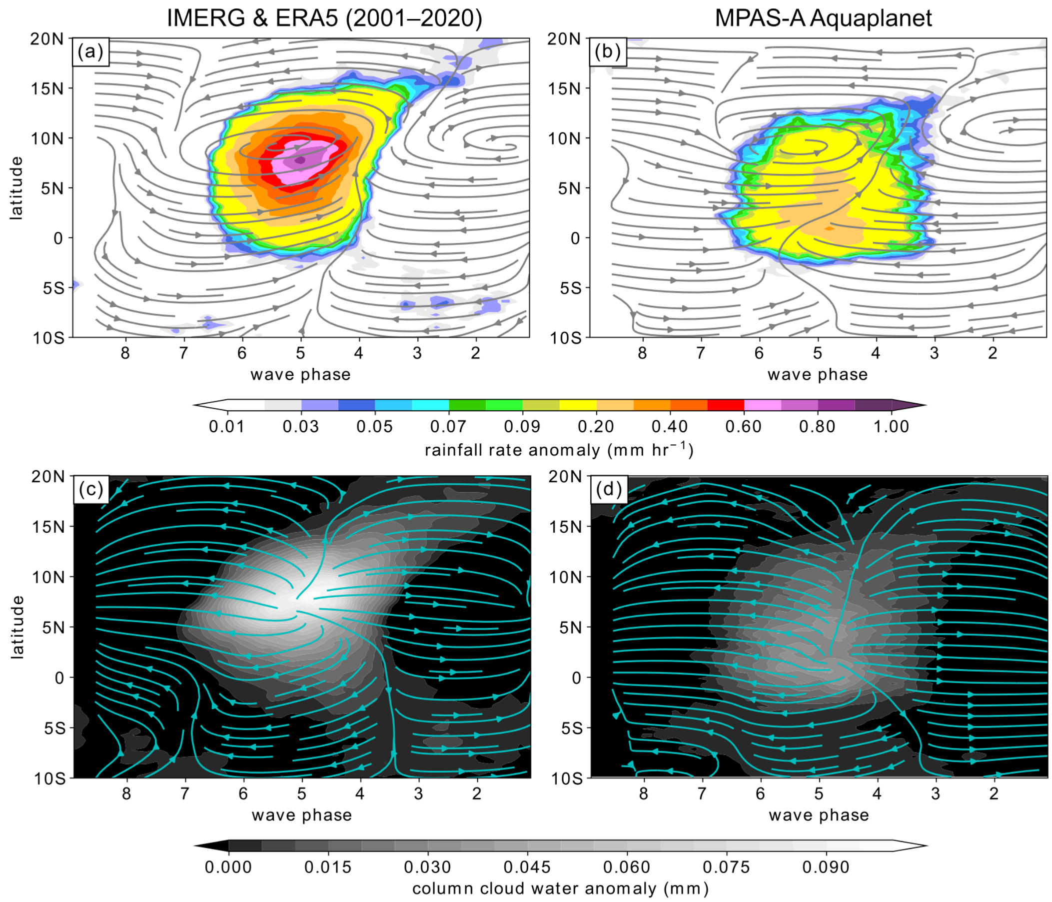

Figure 12. As in Fig. 10, except for easterly waves.

difference could be due to a number of reasons, including the different sample sizes and the different reference background (the time-mean climatology from MPAS-A, but the annual and seasonal cycle from ERA5 and IMERG). Another plausible reason is that MPAS-A with convection-permitting resolution has a stronger convection-circulation coupling than ERA5 (which relies on a convection parameterization).

The aquaplanet simulation also captures the overall structure of easterly waves (Figs. 12–13). Anomalous lower-tropospheric cyclonic winds appear to the west of the convectively active phase (phases 8–5) and overlap with the heaviest rainfall and cloudiest regions of these waves (Figs. 12a,b). Anomalous upper-tropospheric westerlies appear to the west of the rainfall and clouds (i.e., phases 8–5), whereas upper-tropospheric easterlies appear to the east (i.e., phases 4–2) (Figs. 12c,d). Notably, the simulated easterly waves are weaker than their observed counterparts. The rainfall rate and cloud water anomalies are half as strong in the aquaplanet than in IMERG and ERA5, respectively. This is in contrast to Kelvin waves, which are substantially stronger in MPAS-A than in observations. Also, the heaviest rainfall anomalies appear to the south of the cyclonic winds in the aquaplanet instead of being co-located with the cyclonic winds as in IMERG/ERA5. This contrasting structure could be due to the overall southward shift of rainfall in MPAS-A than in observations (Fig. 3e-f).

The vertical cross sections reveal an overall consistent structure between the aquaplanet and reanalysis. Weak temperature anomalies appear in both ERA5 and MPAS-A (Fig. 13a,b). A "boomerang" type pattern exists above 800 hPa, where warm anomalies tilt eastward with height up to 250 hPa and then tilt westward with height aloft. This pattern was noted by Serra et al. (2008) for Pacific ocean easterly waves. Likewise, easterly waves are associated with pronounced water vapor anomalies (Fig. 13c,d). Moist lower-tropospheric anomalies appear to the west of the peak rainfall (phases 8–5) and moist upper-tropospheric anomalies appear during and to the east of the rainfall peak (phases 5–3). These waves are also associated with pronounced meridional wind anomalies, with anomalous northerlies located to the west of the rainfall peak and anomalous southerlies to the east of the rainfall peak from the surface up to 400 hPa (Fig. 13a,b). These anomalies are characteristic of the rotational flow associated with easterly waves (Figs. 10a,b), which is confirmed with the anomalous cyclonic relative vorticity anomalies (Fig. 13c,d). A reversed pattern of meridional winds exists above 400 hPa, characterized by anomalous southerlies to the west of the rainfall peak and anomalous northerlies to the east.

A key difference between observed and simulated easterly waves is the height of their strongest meridional wind and vorticity anomalies. While the strongest meridional wind anomalies appear around 800 hPa in ERA5, the strongest meridional winds appear around 700 hPa in the aquaplanet simulation. A broad cyclonic vorticity vorcity anomaly extends from 850 hPa to 400 hPa in ERA5, which is likely a combination of the characteristic lower-tropospheric vorticity maximum of west Pacific easterly waves and the midtropospheric vorticity maximum of east Pacific easterly waves (Serra et al., 2008). However, the aquaplanet simulation exhibits a single anomaly centered between 600–500 hPa. These differences likely stem from the different base states (Section 3.1) as previous studies suggest that the structure of Pacific easterly waves is highly sensitive to the background winds (e.g., Serra et al., 2008; Rydbeck & Maloney, 2014).

Notwithstanding these differences, MPAS-A also captures other key features of the easterly waves. Anomalous ascent is evident throughout most of the troposphere during the convectively active phase (Fig. 13e,f). This anomalous ascent is accompanied by anomalous lower-tropospheric convergence and anomalous upper-tropospheric divergence (Fig. 13e,f). A slight eastward tilt with height is evident in the water vapor, vorticity, convergence, and vertical motion fields. The maximum anomalous ascent appears above 500 hPa in both datasets, but the peak ascent is weaker in MPAS-A than in ERA5. Anomalously dry conditions, downward motion, and lower-tropospheric divergence exist during the convectively suppressed phase of these waves (phases 3–1), as expected.

Intriguingly, the structure of easterly waves is more realistic in this aquaplanet experiment than in the aquaplanet experiment of Rios-Berrios et al. (2023). We attribute these more realistic structures to the underlying SST profile. Rios-Berrios et al. (2023) used an SST profile that peaks at the equator, whereas the profile used here has a maximum SST at 10°N. The profile used here is a more realistic representation of Northern Hemisphere summer conditions that support these waves in nature. Furthermore, the mean circulation in the aquaplanet experiment is controlled primarily by the fixed SST profile. The mean circulation in these experiments is characterized by a time mean, zonal mean rainfall peak in the Northern Hemisphere (Fig. 3c). Likewise, the mean vertical wind shear between 0–20 N is approximately 3–5 m s $^{-1}$ weaker in these experiments than in the experiments with the peak SST at the equator. All these factors could yield different background conditions, which likely affects the structure of simulated easterly waves. A future study will examine these possibilities through parallel analyses and theoretical considerations of the easterly waves in both simulations.

4 Summary and Conclusions

This study documents a novel aquaplanet experiment with convection-permitting resolution in the tropics. The experiment was produced with the Model for Prediction Across Scales-Atmosphere (MPAS-A), and it was designed to study multi-scale interac-

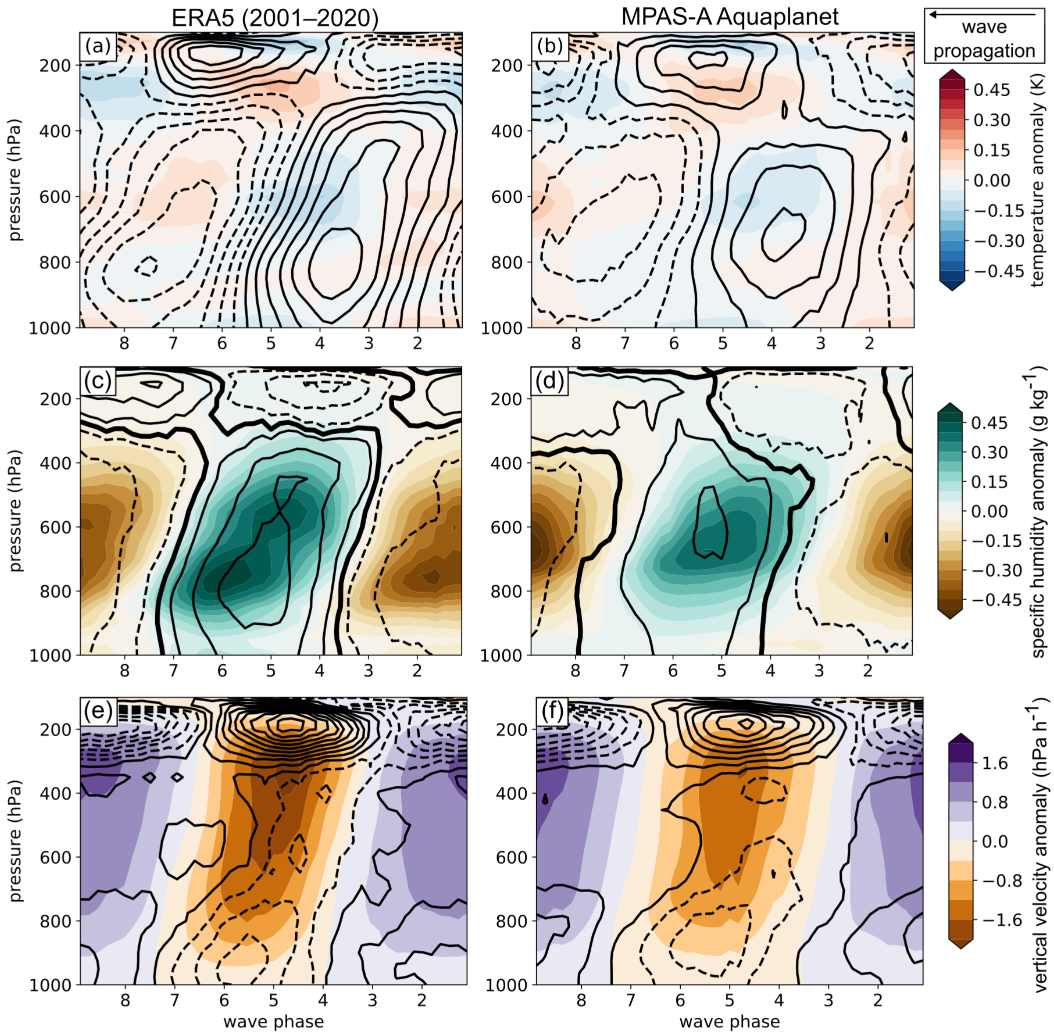

Figure 13. Pressure-wave phase composites anomalies associated with easterly waves in (a,c,e) ERA5/IMERG and (b,d,f) MPAS-A. Panels show (a-b) temperature (shading, every 0.05 K) and *meridional* wind (contours, every 0.2 m s^{-1}), (c-d) specific humidity (shading, every 0.05 g kg^{-1}) and relative vorticity (contours, every 0.1×10^{-5} s^{-1}), and (e-f) vertical velocity (shading, every 0.4 hPa h^{-1}) and divergence (contours,every 0.05×10^{-5} s^{-1}). In all panels, solid contours represent positive anomalies, dashed contours represent negative anomalies, and thick lines denote the zero contour.

tions leading to tropical cyclogenesis. A variable resolution mesh was used to employ 3-km cell spacing between 10°S and 30°N with a transition to approximately 12.3-km cell spacing poleward of 30°S and 55°N. This hemispheric asymmetric configuration overlaps with an SST profile that peaks at 10°N. The simulation was integrated for 160 days, but the first 30 days were considered model spin up and the analysis focused on the last 130 days.

Despite being a highly idealized framework, the simulation captures many of the expected features of a tropical atmosphere. The tropical mean state is characterized by warm and moist air that ascends within the rising branch of a Hadley cell. Easterly winds extend from the surface up to the upper troposphere, where the winds turn into westerlies and yield westerly wind shear. Most TCs form within favorable large-scale conditions, although a distribution of cyclogenesis location also shows that some TCs develop poleward of 20°N. Visual inspection of model output (not shown) led us to conclude that the second group of TCs form through the "tropical transition" pathway (McTaggart-Cowan et al., 2008) along frontal zones of midlatitude cyclones.

The simulated TCs evolve consistently with their observed counterparts. Most cyclones develop in the deep tropics, travel west-northwestward while intensifying, and dissipate or transition into extratropical cyclones. The simulation captures 23 major hurricanes, which demonstrates that convection-permitting resolution improves the statistics of simulated TCs as previous aquaplanet experiments with coarser resolution than ours did not capture major hurricanes. A comparison against multi-year dropsonde composites confirmed that the simulated TC structure is also consistent with observations across all stages—from weak tropical storm to major hurricane stage. A noteworthy discrepancy between simulated and observed TCs was that the height of the warm core appeared at a lower altitude in the aquaplanet simulation than in the dropsonde composite, but this could stem from relatively small samples of high-altitude dropsonde data in the inner core of major hurricanes.

The simulation also captures the overall structure of equatorial waves. Rainfall rates averaged between 5°S–10°N showed substantial rainfall variability predominantly associated with eastward-propagating Kelvin waves. Smaller-scale, shorter-lived rainfall features also exist, and those are primarily associated with easterly waves. The vertical structure of simulated Kelvin and easterly waves is consistent with their observed counterparts, as demonstrated by a comparison against Pacific Ocean Kelvin and easterly waves in satellite and reanalysis data. Both types of waves are associated with substantial kinematic and thermodynamic anomalies that could influence the environmental and local conditions during tropical cyclogenesis.

We conclude that the simulation is suitable for process-based and statistical studies of TCs, including tropical cyclogenesis. A major benefit of this simulation is that it captures the complete lifecycle of over 100 TCs and multiple equatorial waves. Both phenomena develop spontaneously via the model physics—that is, we do not impose an initial TC vortex or equatorial wave structure. Therefore, the simulation is able to represent the evolution of those phenomena through the model equations and physics parameterizations. A future study will examine the relationship between tropical cyclogenesis and equatorial Kelvin waves. Future studies may also consider exploiting this powerful dataset to explore other aspects of TCs. However, any future study should consider the limitations of this simulation, including the relatively short integration time and the absence of atmosphere-ocean feedback.

5 Open Research

The original model output is too large to publicly archive; instead, we provide a public dataset containing the interpolated model output used in this study (Rios-Berrios, 2023). Additionally, the model code with modifications to use the aquaplanet framework and other supporting files are provided by Rios-Berrios (2022). The IMERG dataset was provided by NASA via `https://disc.gsfc.nasa.gov/`, the ERA5 dataset was provided by NCAR's Research Data Archive (European Centre for Medium-Range Weather Forecasts, 2019), and the IBTRACs dataset was provided by NOAA's National Centers for Environmental Information (Knapp et al., 2018).

Acknowledgments

The authors would like to thank Dr. Kevin Hodges for providing and assisting with the TRACK algorithm, and Dr. Falko Judt for providing code to refine the TC tracks used in this study. The authors also thank Dr. George Bryan and Dr. Brian Medeiros for insightful comments about this study. The authors acknowledge high-performance computing support from Cheyenne (doi:10.5065/D6RX99HX) provided by NCAR's Computational and Information Systems Laboratory. This material is based upon work supported by NCAR, which is a major facility sponsored by the National Science Foundation under Cooperative Agreement No. 1852977.

References

Andersen, J. A., & Kuang, Z. (2012). Moist static energy budget of mjo-like disturbances in the atmosphere of a zonally symmetric aquaplanet. *J. Climate*, *25*(8), 2782 - 2804. doi: 10.1175/JCLI-D-11-00168.1

Ballinger, A. P., Merlis, T. M., Held, I. M., & Zhao, M. (2015, June). The Sensitivity of Tropical Cyclone Activity to Off-Equatorial Thermal Forcing in Aquaplanet Simulations. *J. Atmos. Sci.*, *72*(6), 2286–2302. Retrieved from `http://journals.ametsoc.org/doi/10.1175/JAS-D-14-0284.1` doi: 10.1175/JAS-D-14-0284.1

Bengtsson, L., Hodges, K. I., & Esch, M. (2007, January). Tropical cyclones in a t159 resolution global climate model: comparison with observations and reanalyses. *Tellus*, *59*(4), 396. Retrieved from `https://doi.org/10.1111/j.1600-0870.2007.00236.x` doi: 10.1111/j.1600-0870.2007.00236.x

Bengtsson, L., Hodges, K. I., Esch, M., Keenlyside, N., Kornblueh, L., Luo, J.-J., & Yamagata, T. (2007, January). How may tropical cyclones change in a warmer climate? *Tellus*, *59*(4), 539. Retrieved from `https://doi.org/10.1111/j.1600-0870.2007.00251.x` doi: 10.1111/j.1600-0870.2007.00251.x

Bessafi, M., & Wheeler, M. C. (2006, February). Modulation of South Indian Ocean Tropical Cyclones by the Madden–Julian Oscillation and Convectively Coupled Equatorial Waves. *Mon. Wea. Rev.*, *134*(2), 638–656. Retrieved 2016-12-28, from `http://journals.ametsoc.org/doi/abs/10.1175/MWR3087.1` doi: 10.1175/MWR3087.1

Blackburn, M., & Hoskins, B. J. (2013). Context and aims of the aqua-planet experiment. *J. Meteor. Soc. Jpn.*, *91A*, 1-15. doi: 10.2151/jmsj.2013-A01

Blackburn, M., Williamson, D. L., Nakajima, K., Ohfuchi, W., Takahashi, Y. O., Hayashi, Y.-Y., ... Stratton, R. (2013). The Aqua-Planet Experiment (APE): CONTROL SST Simulation. *J. Meteor. Soc. Jpn.*, *91A*(0), 17–56. doi: 10.2151/jmsj.2013-A02

Burnett, A. C., Sheshadri, A., Silvers, L. G., & Robinson, T. (2021, March). Tropical cyclone frequency under varying SSTs in aquaplanet simulations. *Geophys. Res. Lett.*, *48*(5). Retrieved from `https://doi.org/10.1029/2020gl091980` doi: 10.1029/2020gl091980

Chavas, D. R., Reed, K. A., & Knaff, J. A. (2017, November). Physical understanding of the tropical cyclone wind-pressure relationship. *Nature Comm.*, *8*(1). Retrieved from `https://doi.org/10.1038/s41467-017-01546-9` doi: 10.1038/s41467-017-01546-9

Das, S., Sengupta, D., Chakraborty, A., Sukhatme, J., & Murtugudde, R. (2016, April). Low-frequency intraseasonal variability in a zonally symmetric aquaplanet model. *Meteor. Atmos. Phys.*, *128*(6), 697–713. Retrieved from https://doi.org/10.1007/s00703-016-0448-y doi: 10.1007/s00703-016-0448-y

European Centre for Medium-Range Weather Forecasts. (2019). *Era5 reanalysis (0.25 degree latitude-longitude grid).* Boulder CO: Research Data Archive at the National Center for Atmospheric Research, Computational and Information Systems Laboratory. Retrieved from https://doi.org/10.5065/BH6N-5N20

Frank, W. M., & Roundy, P. E. (2006, September). The Role of Tropical Waves in Tropical Cyclogenesis. *Mon. Wea. Rev.*, *134*(9), 2397–2417. Retrieved 2015-03-19, from http://journals.ametsoc.org/doi/abs/10.1175/MWR3204.1 doi: 10.1175/MWR3204.1

Frierson, D. M. W. (2007, June). Convectively Coupled Kelvin Waves in an Idealized Moist General Circulation Model. *J. Atmos. Sci.*, *64*(6), 2076–2090. doi: 10.1175/JAS3945.1

Frierson, D. M. W., Kim, D., Kang, I.-S., Lee, M.-I., & Lin, J. (2011, January). Structure of AGCM-Simulated Convectively Coupled Kelvin Waves and Sensitivity to Convective Parameterization. *J. Atmos. Sci.*, *68*(1), 26–45. doi: 10.1175/2010JAS3356.1

Gray, W. M. (1968, October). Global View of the Origin of Tropical Disturbances and Storms. *Mon. Wea. Rev.*, *96*(10), 669–700.

Hall, J. D., Matthews, A. J., & Karoly, D. J. (2001, December). The modulation of tropical cyclone activity in the australian region by the madden–julian oscillation. *Mon. Wea. Rev.*, *129*(12), 2970–2982. Retrieved from https://doi.org/10.1175/1520-0493(2001)129<2970:tmotca>2.0.co;2 doi: 10.1175/1520-0493(2001)129⟨2970:tmotca⟩2.0.co;2

Hayashi, Y.-Y., & Sumi, A. (1986). The 30-40 Day Oscillations Simulated in an "Aqua Planet" Model. *J. Meteor. Soc. Jpn.*, *64*(4), 451–467. doi: 10.2151/jmsj1965.64.4_451

Held, I. M., & Suarez, M. J. (1994, October). A Proposal for the Intercomparison of the Dynamical Cores of Atmospheric General Circulation Models. *Bull. Amer. Meteor. Soc.*, *75*(10), 1825–1830. doi: 10.1175/1520-0477(1994)075⟨1825:APFTIO⟩2.0.CO;2

Hersbach, H., Bell, B., Berrisford, P., Hirahara, S., Horányi, A., Muñoz-Sabater, J., … Thépaut, J.-N. (2020). The ERA5 global reanalysis. *Q. J. R. Meteor. Soc.*, *146*(730), 1999–2049. doi: 10.1002/qj.3803

Hess, P. G., Battisti, D. S., & Rasch, P. J. (1993, March). Maintenance of the Intertropical Convergence Zones and the Large-Scale Tropical Circulation on a Water-covered Earth. *J. Atmos. Sci.*, *50*(5), 691–713. doi: 10.1175/1520-0469(1993)050⟨0691:MOTICZ⟩2.0.CO;2

Hodges, K., Cobb, A., & Vidale, P. L. (2017, July). How well are tropical cyclones represented in reanalysis datasets? *J. Climate*, *30*(14), 5243–5264. Retrieved from https://doi.org/10.1175/jcli-d-16-0557.1 doi: 10.1175/jcli-d-16-0557.1

Hodges, K. I. (1996, December). Spherical nonparametric estimators applied to the UGAMP model integration for AMIP. *Mon. Wea. Rev.*, *124*(12), 2914–2932. Retrieved from https://doi.org/10.1175/1520-0493(1996)124<2914:sneatt>2.0.co;2 doi: 10.1175/1520-0493(1996)124⟨2914:sneatt⟩2.0.co;2

Hodges, K. I. (1999, June). Adaptive constraints for feature tracking. *Mon. Wea. Rev.*, *127*(6), 1362–1373. Retrieved from https://doi.org/10.1175/1520-0493(1999)127<1362:acfft>2.0.co;2 doi: 10.1175/1520-0493(1999)127⟨1362:acfft⟩2.0.co;2

Hong, S.-Y., Dudhia, J., & Chen, S.-H. (2004, January). A Revised Approach to Ice Microphysical Processes for the Bulk Parameterization of Clouds and Precipitation. *Mon. Wea. Rev.*, *132*(1), 103–120. doi: 10.1175/1520-0493(2004)132⟨0103:ARATIM⟩2.0.CO;2

Hong, S.-Y., Noh, Y., & Dudhia, J. (2006, September). A New Vertical Diffusion Package with an Explicit Treatment of Entrainment Processes. *Mon. Wea. Rev.*, *134*(9), 2318–2341. doi: 10.1175/MWR3199.1

Huffman, G. J., Bolvin, D. T., Nelkin, E. J., & Tan, J. (2019, September). *Integrated Multi-satellitE Retrievals for GPM (IMERG) Technical Documentation.* National Aeronautics and Space Administration. Retrieved 2019-12-20, from https://docserver.gesdisc.eosdis.nasa.gov/public/project/GPM/IMERG_doc.06.pdf

Iacono, M. J., Delamere, J. S., Mlawer, E. J., Shephard, M. W., Clough, S. A., & Collins, W. D. (2008, July). Radiative forcing by long-lived greenhouse gases: Calculations with the AER radiative transfer models. *J. Geophys. Res.*, *113*(D13). doi: 10.1029/2008JD009944

Jones, P. W. (1999, September). First- and second-order conservative remapping schemes for grids in spherical coordinates. *Mon. Wea. Rev.*, *127*(9), 2204–2210. Retrieved from https://doi.org/10.1175/1520-0493(1999)127<2204:fasocr>2.0.co;2 doi: 10.1175/1520-0493(1999)127⟨2204:fasocr⟩2.0.co;2

Judt, F., Klocke, D., Rios-Berrios, R., Vanniere, B., Ziemen, F., Auger, L., … Zhou, L. (2021). Tropical Cyclones in Global Storm-Resolving Models. *J. Meteor. Soc. Jpn.*, *99*(3), 579–602. Retrieved from https://www.jstage.jst.go.jp/article/jmsj/99/3/99_2021-029/_article doi: 10.2151/jmsj.2021-029

Judt, F., & Rios-Berrios, R. (2021, July). Resolved Convection Improves the Representation of Equatorial Waves and Tropical Rainfall Variability in a Global Nonhydrostatic Model. *Geophys. Res. Lett.*, *48*(14). Retrieved 2021-09-25, from https://onlinelibrary.wiley.com/doi/10.1029/2021GL093265 doi: 10.1029/2021GL093265

Jung, H., & Knippertz, P. (2023, January). Link between the time-space behavior of rainfall and 3d dynamical structures of equatorial waves in global convection-permitting simulations. *Geophys. Res. Lett.*, *50*(2). Retrieved from https://doi.org/10.1029/2022gl100973 doi: 10.1029/2022gl100973

Kiladis, G. N., Wheeler, M. C., Haertel, P. T., Straub, K. H., & Roundy, P. E. (2009, June). Convectively Coupled Equatorial Waves. *Rev. Geophys.*, *47*(2), RG2003. doi: 10.1029/2008RG000266

Kim, J.-H., Ho, C.-H., Kim, H.-S., Sui, C.-H., & Park, S. K. (2008, March). Systematic variation of summertime tropical cyclone activity in the western north pacific in relation to the madden–julian oscillation. *J. Climate*, *21*(6), 1171–1191. Retrieved from https://doi.org/10.1175/2007jcli1493.1 doi: 10.1175/2007jcli1493.1

Klotzbach, P. J. (2010, January). On the madden–julian oscillation–atlantic hurricane relationship. *J. Climate*, *23*(2), 282–293. Retrieved from https://doi.org/10.1175/2009jcli2978.1 doi: 10.1175/2009jcli2978.1

Klotzbach, P. J., & Oliver, E. C. J. (2014, December). Modulation of atlantic basin tropical cyclone activity by the madden–julian oscillation (MJO) from 1905 to 2011. *J. Climate*, *28*(1), 204–217. Retrieved from https://doi.org/10.1175/jcli-d-14-00509.1 doi: 10.1175/jcli-d-14-00509.1

Klotzbach, P. J., & Oliver, E. C. J. (2015, May). Variations in global tropical cyclone activity and the madden-julian oscillation since the midtwentieth century. *Geophys. Res. Lett.*, *42*(10), 4199–4207. Retrieved from https://doi.org/10.1002/2015gl063966 doi: 10.1002/2015gl063966

Knapp, K. R., Diamond, H. J., Kossin, J. P., Kruk, M. C., & Schreck, C. J. (2018). *International best track archive for climate stewardship (ibtracs) project, version 4.* NOAA National Centers for Environmental Information. Retrieved from https://data.nodc.noaa.gov/cgi-bin/iso?id=gov.noaa.ncdc:

C01552 doi: 10.25921/82TY-9E16

Knapp, K. R., Kruk, M. C., Levinson, D. H., Diamond, H. J., & Neumann, C. J. (2010, March). The international best track archive for climate stewardship (IBTrACS). *Bull. Amer. Meteorol. Soc.*, *91*(3), 363–376. Retrieved from https://doi.org/10.1175/2009bams2755.1 doi: 10.1175/2009bams2755.1

Kossin, J. P., Emanuel, K. A., & Vecchi, G. A. (2014, May). The poleward migration of the location of tropical cyclone maximum intensity. *Nature*, *509*(7500), 349–352. Retrieved from https://doi.org/10.1038/nature13278 doi: 10.1038/nature13278

Lawton, Q. A., Majumdar, S. J., Dotterer, K., Thorncroft, C., & Schreck, C. J. (2022, August). The influence of convectively coupled kelvin waves on african easterly waves in a wave-following framework. *Mon. Wea. Rev.*, *150*(8), 2055–2072. Retrieved from https://doi.org/10.1175/mwr-d-21-0321.1 doi: 10.1175/mwr-d-21-0321.1

MacDonald, C. G., & Ming, Y. (2022, December). Tropical intraseasonal variability response to zonally asymmetric forcing in an idealized moist GCM. *J. Climate*, *35*(24), 4479–4501. Retrieved from https://doi.org/10.1175/jcli-d-22-0344.1 doi: 10.1175/jcli-d-22-0344.1

Maher, P., Gerber, E. P., Medeiros, B., Merlis, T. M., Sherwood, S., Sheshadri, A., … Zurita-Gotor, P. (2019, June). Model Hierarchies for Understanding Atmospheric Circulation. *Rev. Geophys.*, *57*(2), 250–280. doi: 10.1029/2018RG000607

Maloney, E. D., & Hartmann, D. L. (2000, May). Modulation of eastern north pacific hurricanes by the madden–julian oscillation. *J. Climate*, *13*(9), 1451–1460. Retrieved from https://doi.org/10.1175/1520-0442(2000)013<1451:moenph>2.0.co;2 doi: 10.1175/1520-0442(2000)013⟨1451:moenph⟩2.0.co;2

Maloney, E. D., & Hartmann, D. L. (2001, September). The madden–julian oscillation, barotropic dynamics, and north pacific tropical cyclone formation. part i: Observations. *J. Atmos. Sci.*, *58*(17), 2545–2558. Retrieved from https://doi.org/10.1175/1520-0469(2001)058<2545:tmjobd>2.0.co;2 doi: 10.1175/1520-0469(2001)058⟨2545:tmjobd⟩2.0.co;2

Maloney, E. D., & Shaman, J. (2008, June). Intraseasonal Variability of the West African Monsoon and Atlantic ITCZ. *J. Climate*, *21*(12), 2898–2918. Retrieved 2015-06-27, from http://journals.ametsoc.org/doi/abs/10.1175/2007JCLI1999.1 doi: 10.1175/2007JCLI1999.1

McTaggart-Cowan, R., Deane, G. D., Bosart, L. F., Davis, C. A., & Galarneau, T. J. (2008, April). Climatology of tropical cyclogenesis in the north atlantic (1948–2004). *Mon. Wea. Rev.*, *136*(4), 1284–1304. Retrieved from https://doi.org/10.1175/2007mwr2245.1 doi: 10.1175/2007mwr2245.1

Medeiros, B., Clement, A. C., Benedict, J. J., & Zhang, B. (2021, March). Investigating the impact of cloud-radiative feedbacks on tropical precipitation extremes. *Climate Atmos. Sci.*, *4*(1). Retrieved from https://doi.org/10.1038/s41612-021-00174-x doi: 10.1038/s41612-021-00174-x

Medeiros, B., & Stevens, B. (2011, January). Revealing differences in GCM representations of low clouds. *Climate Dyn.*, *36*(1-2), 385–399. doi: 10.1007/s00382-009-0694-5

Merlis, T. M., & Held, I. M. (2019, September). Aquaplanet Simulations of Tropical Cyclones. *Curr. Climate Change Rep.*, *5*(3), 185–195. doi: 10.1007/s40641-019-00133-y

Merlis, T. M., Zhao, M., & Held, I. M. (2013, August). The Sensitivity of Hurricane Frequency to ITCZ Changes and Radiatively Forced Warming in Aquaplanet Simulations. *Geophys. Res. Lett.*, *40*(15), 4109–4114. Retrieved 2016-12-29, from http://doi.wiley.com/10.1002/grl.50680 doi: 10.1002/grl.50680

Merlis, T. M., Zhou, W., Held, I. M., & Zhao, M. (2016, March). Surface temperature dependence of tropical cyclone-permitting simulations in a spherical model with uniform thermal forcing. *Geophys. Res. Lett.*, *43*(6), 2859–2865. Retrieved from https://doi.org/10.1002/2016gl067730 doi: 10.1002/2016gl067730

Miura, H., Tomita, H., Nasuno, T., Iga, S.-i., Satoh, M., & Matsuno, T. (2005, October). A climate sensitivity test using a global cloud resolving model under an aqua planet condition. *Geophys. Res. Lett.*, *32*(19). doi: 10.1029/2005GL023672

Nakajima, K., Yamada, Y., Takahashi, Y. O., Ishiwatari, M., Ohfuchi, W., & Hayashi, Y.-Y. (2013). The Variety of Spontaneously Generated Tropical Precipitation Patterns Found in APE Results. *J. Meteor. Soc. Jpn.*, *91A*(0), 91–141. doi: 10.2151/jmsj.2013-A04

Narenpitak, P., Bretherton, C. S., & Khairoutdinov, M. F. (2020, July). The role of multiscale interaction in tropical cyclogenesis and its predictability in near-global aquaplanet cloud-resolving simulations. *J. Atmos. Sci.*, *77*(8), 2847–2863. Retrieved from https://doi.org/10.1175/jas-d-20-0021.1 doi: 10.1175/jas-d-20-0021.1

Nasuno, T., Tomita, H., Iga, S., Miura, H., & Satoh, M. (2007, June). Multiscale Organization of Convection Simulated with Explicit Cloud Processes on an Aquaplanet. *J. Atmos. Sci.*, *64*(6), 1902–1921. Retrieved from https://journals.ametsoc.org/doi/10.1175/JAS3948.1 doi: 10.1175/JAS3948.1

Nasuno, T., Tomita, H., Iga, S., Miura, H., & Satoh, M. (2008, April). Convectively Coupled Equatorial Waves Simulated on an Aquaplanet in a Global Nonhydrostatic Experiment. *J. Atmos. Sci.*, *65*(4), 1246–1265. Retrieved from http://journals.ametsoc.org/doi/abs/10.1175/2007JAS2395.1 doi: 10.1175/2007JAS2395.1

Nguyen, L. T., Molinari, J., & Thomas, D. (2014, November). Evaluation of Tropical Cyclone Center Identification Methods in Numerical Models. *Mon. Wea. Rev.*, *142*(11), 4326–4339. Retrieved 2017-06-13, from http://journals.ametsoc.org/doi/abs/10.1175/MWR-D-14-00044.1 doi: 10.1175/MWR-D-14-00044.1

Reed, K. A., & Chavas, D. R. (2015, December). Uniformly rotating global radiative-convective equilibrium in the community atmosphere model, version 5. *J. Adv. Model. Earth Sys.*, *7*(4), 1938–1955. Retrieved from https://doi.org/10.1002/2015ms000519 doi: 10.1002/2015ms000519

Riley, E. M., Mapes, B. E., & Tulich, S. N. (2011, December). Clouds associated with the madden–julian oscillation: A new perspective from CloudSat. *J. Atmos. Sci.*, *68*(12), 3032–3051. Retrieved from https://doi.org/10.1175/jas-d-11-030.1 doi: 10.1175/jas-d-11-030.1

Rios-Berrios, R. (2022). *Mpas-a v6.2 with modifications to use the aquaplanet capability.* Zenodo. Retrieved from https://zenodo.org/record/6323189 doi: 10.5281/ZENODO.6323189

Rios-Berrios, R. (2023). *MPAS-A aquaplanet simulation with convection-permitting resolution and off-equatorial SST maximum.* UCAR/NCAR - GDEX. Retrieved from https://gdex.ucar.edu/dataset/id/c5755cab-b90d-40a9-b55c-abb90d60a933.html doi: 10.5065/BVEF-EW68

Rios-Berrios, R., Bryan, G. H., Medeiros, B., Judt, F., & Wang, W. (2022). Differences in tropical rainfall in aquaplanet simulations with resolved or parameterized deep convection. *J. Adv. Model. Earth Sys.*, *14*(5), e2021MS002902. (e2021MS002902 2021MS002902) doi: https://doi.org/10.1029/2021MS002902

Rios-Berrios, R., Judt, F., Bryan, G. H., Medeiros, B., & Wang, W. (2023). Three-dimensional structure of convectively coupled equatorial waves in aquaplanet experiments with resolved or parameterized convection. *J. Climate, in press*. doi: 10.1175/JCLI-D-22-0422.1

Rios-Berrios, R., Medeiros, B., & Bryan, G. H. (2020, September). Mean Climate and Tropical Rainfall Variability in Aquaplanet Simulations using the Model for Prediction Across Scales – Atmosphere. *J. Adv. Model. Earth Syst.*. doi: 10.1029/2020MS002102

Roberts, M. J., Camp, J., Seddon, J., Vidale, P. L., Hodges, K., Vanniere, B., ... Ullrich, P. (2020, April). Impact of model resolution on tropical cyclone simulation using the HighResMIP–PRIMAVERA multimodel ensemble. *J. Climate*, *33*(7), 2557–2583. Retrieved from `https://doi.org/10.1175/jcli-d-19-0639.1` doi: 10.1175/jcli-d-19-0639.1

Roundy, P. E. (2008). Analysis of convectively coupled kelvin waves in the indian ocean mjo. *J. Atmos. Sci.*, *65*(4), 1342 - 1359. doi: 10.1175/2007JAS2345.1

Rydbeck, A. V., & Maloney, E. D. (2014, October). Energetics of east pacific easterly waves during intraseasonal events. *J. Climate*, *27*(20), 7603–7621. Retrieved from `https://doi.org/10.1175/jcli-d-14-00211.1` doi: 10.1175/jcli-d-14-00211.1

Sakaeda, N., Kiladis, G., & Dias, J. (2020, April). The diurnal cycle of rainfall and the convectively coupled equatorial waves over the maritime continent. *J. Climate*, *33*(8), 3307–3331. Retrieved from `https://doi.org/10.1175/jcli-d-19-0043.1` doi: 10.1175/jcli-d-19-0043.1

Schlueter, A., Fink, A. H., Knippertz, P., & Vogel, P. (2019, March). A Systematic Comparison of Tropical Waves over Northern Africa. Part I: Influence on Rainfall. *J. Climate*, *32*(5), 1501–1523. Retrieved from `https://journals.ametsoc.org/jcli/article/32/5/1501/89187/A-Systematic-Comparison-of-Tropical-Waves-over` doi: 10.1175/JCLI-D-18-0173.1

Schreck, C. J. (2015, July). Kelvin Waves and Tropical Cyclogenesis: A Global Survey. *Mon. Wea. Rev.*, *143*(10), 3996–4011. doi: 10.1175/MWR-D-15-0111.1

Schreck, C. J. (2016, September). Convectively Coupled Kelvin Waves and Tropical Cyclogenesis in a Semi-Lagrangian Framework. *Mon. Wea. Rev.*, *144*(11), 4131–4139. doi: 10.1175/MWR-D-16-0237.1

Schreck, C. J., Molinari, J., & Aiyyer, A. (2011, September). A Global View of Equatorial Waves and Tropical Cyclogenesis. *Mon. Wea. Rev.*, *140*(3), 774–788. Retrieved 2016-12-20, from `http://journals.ametsoc.org/doi/abs/10.1175/MWR-D-11-00110.1` doi: 10.1175/MWR-D-11-00110.1

Schreck, C. J., Molinari, J., & Mohr, K. I. (2010, October). Attributing Tropical Cyclogenesis to Equatorial Waves in the Western North Pacific. *J. Atmos. Sci.*, *68*(2), 195–209. doi: 10.1175/2010JAS3396.1

Schulzweida, U. (2022, October). *Cdo user guide.* Zenodo. Retrieved from `https://doi.org/10.5281/zenodo.7112925` doi: 10.5281/zenodo.7112925

Serra, Y. L., Kiladis, G. N., & Cronin, M. F. (2008, April). Horizontal and vertical structure of easterly waves in the pacific ITCZ. *J. Atmos. Sci.*, *65*(4), 1266–1284. Retrieved from `https://doi.org/10.1175/2007jas2341.1` doi: 10.1175/2007jas2341.1

Shi, X., & Bretherton, C. S. (2014, July). Large-scale character of an atmosphere in rotating radiative-convective equilibrium. *J. Adv. Model. Earth Sys.*, *6*(3), 616–629. Retrieved from `https://doi.org/10.1002/2014ms000342` doi: 10.1002/2014ms000342

Skamarock, W. C., Klemp, J. B., Duda, M. G., Fowler, L. D., Park, S.-H., & Ringler, T. D. (2012, April). A Multiscale Nonhydrostatic Atmospheric Model Using Centroidal Voronoi Tesselations and C-Grid Staggering. *Mon. Wea. Rev.*, *140*(9), 3090–3105. doi: 10.1175/MWR-D-11-00215.1

Stansfield, A. M., & Reed, K. A. (2021, December). Tropical cyclone precipitation response to surface warming in aquaplanet simulations with uniform thermal forcing. *J. Geophys. Res. Atmos.*, *126*(24). Retrieved from `https://doi.org/10.1029/2021jd035197` doi: 10.1029/2021jd035197

Stern, D. P., & Nolan, D. S. (2012, May). On the height of the warm core in tropical cyclones. *J. Atmos. Sci.*, *69*(5), 1657–1680. Retrieved from https://doi.org/10.1175/jas-d-11-010.1 doi: 10.1175/jas-d-11-010.1

Stevens, B., Satoh, M., Auger, L., Biercamp, J., Bretherton, C. S., Chen, X., … Zhou, L. (2019, December). DYAMOND: the DYnamics of the Atmospheric general circulation Modeled On Non-hydrostatic Domains. *Prog. Earth Planet. Sc.*, *6*(1). doi: 10.1186/s40645-019-0304-z

Strachan, J., Vidale, P. L., Hodges, K., Roberts, M., & Demory, M.-E. (2013, January). Investigating global tropical cyclone activity with a hierarchy of AGCMs: The role of model resolution. *J. Climate*, *26*(1), 133–152. Retrieved from https://doi.org/10.1175/jcli-d-12-00012.1 doi: 10.1175/jcli-d-12-00012.1

Straub, K. H., & Kiladis, G. N. (2003, July). The Observed Structure of Convectively Coupled Kelvin Waves: Comparison with Simple Models of Coupled Wave Instability. *J. Atmos. Sci.*, *60*(14), 1655–1668. Retrieved from http://journals.ametsoc.org/doi/abs/10.1175/1520-0469%282003%29060%3C1655%3ATOSOCC%3E2.0.CO%3B2 doi: 10.1175/1520-0469(2003)060⟨1655:TOSOCC⟩2.0.CO;2

Sumi, A. (1992). Pattern Formation of Convective Activity over the Aqua-Planet with Globally Uniform Sea Surface Temperature (SST). *J. Meteor. Soc. Jpn.*, *70*(5), 855–876. doi: 10.2151/jmsj1965.70.5_855

van der Linden, R., Fink, A. H., Pinto, J. G., Phan-Van, T., & Kiladis, G. N. (2016, July). Modulation of daily rainfall in southern vietnam by the madden–julian oscillation and convectively coupled equatorial waves. *J. Climate*, *29*(16), 5801–5820. Retrieved from https://doi.org/10.1175/jcli-d-15-0911.1 doi: 10.1175/jcli-d-15-0911.1

Ventrice, M. J., & Thorncroft, C. D. (2012, October). The Role of Convectively Coupled Atmospheric Kelvin Waves on African Easterly Wave Activity. *Mon. Wea. Rev.*, *141*(6), 1910–1924. doi: 10.1175/MWR-D-12-00147.1

Ventrice, M. J., Thorncroft, C. D., & Schreck, C. J. (2012, March). Impacts of Convectively Coupled Kelvin Waves on Environmental Conditions for Atlantic Tropical Cyclogenesis. *Mon. Wea. Rev.*, *140*(7), 2198–2214. Retrieved 2016-12-20, from http://journals.ametsoc.org/doi/full/10.1175/MWR-D-11-00305.1 doi: 10.1175/MWR-D-11-00305.1

Vu, T.-A., Kieu, C., Chavas, D., & Wang, Q. (2021, January). A numerical study of the global formation of tropical cyclones. *J. Adv. Model. Earth Sys.*, *13*(1). Retrieved from https://doi.org/10.1029/2020ms002207 doi: 10.1029/2020ms002207

Wang, R., & Wu, L. (2019, November). Influence of track changes on the poleward shift of LMI location of western north pacific tropical cyclones. *J. Climate*, *32*(23), 8437–8445. Retrieved from https://doi.org/10.1175/jcli-d-18-0855.1 doi: 10.1175/jcli-d-18-0855.1

Wang, W. (2022, August). Forecasting convection with a “scale-aware” tiedtke cumulus parameterization scheme at kilometer scales. *Wea. Forecasting*, *37*(8), 1491–1507. Retrieved from https://doi.org/10.1175/waf-d-21-0179.1 doi: 10.1175/waf-d-21-0179.1

Webb, M. J., Andrews, T., Bodas-Salcedo, A., Bony, S., Bretherton, C. S., Chadwick, R., … Watanabe, M. (2017, January). The Cloud Feedback Model Intercomparison Project (CFMIP) contribution to CMIP6. *Geosci. Model Develop.*, *10*(1), 359–384. doi: 10.5194/gmd-10-359-2017

Williamson, D. L. (2008, January). Convergence of aqua-planet simulations with increasing resolution in the Community Atmospheric Model, Version 3. *Tellus A*, *60*(5), 848–862. doi: 10.1111/j.1600-0870.2008.00339.x

Williamson, D. L., & Olson, J. G. (2003, April). Dependence of aqua-planet simulations on time step. *Q. J. Roy. Meteor. Soc.*, *129*(591), 2049–2064. doi: 10.1256/qj.02.62

Wu, L., & Takahashi, M. (2017, September). Contributions of tropical waves to tropical cyclone genesis over the western north pacific. *Climate Dynamics*, *50*(11-12), 4635–4649. Retrieved from https://doi.org/10.1007/s00382-017-3895-3 doi: 10.1007/s00382-017-3895-3

Yasunaga, K., & Mapes, B. (2012, January). Differences between more divergent and more rotational types of convectively coupled equatorial waves. part II: Composite analysis based on space–time filtering. *J. Atmos. Sci.*, *69*(1), 17–34. Retrieved from https://doi.org/10.1175/jas-d-11-034.1 doi: 10.1175/jas-d-11-034.1

Zawislak, J., Nguyen, L., Paltz, E., Young, K., Voemel, H., & Hock, T. (2018). Development and applications of a long-term, global tropical cyclone dropsonde dataset. In *33rd conf. on hurricanes and tropical meteorology, ponte vedra, fl.* American Meteorological Society.

Zhang, G., Silvers, L. G., Zhao, M., & Knutson, T. R. (2021, March). Idealized aquaplanet simulations of tropical cyclone activity: Significance of temperature gradients, hadley circulation, and zonal asymmetry. *J. Atmos. Sci.*, *78*(3), 877–902. Retrieved from https://doi.org/10.1175/jas-d-20-0079.1 doi: 10.1175/jas-d-20-0079.1

Zhang, J. A., Rogers, R. F., Nolan, D. S., & Marks, F. D. (2011, August). On the characteristic height scales of the hurricane boundary layer. *Mon. Wea. Rev.*, *139*(8), 2523–2535. Retrieved from https://doi.org/10.1175/mwr-d-10-05017.1 doi: 10.1175/mwr-d-10-05017.1

Zhang, J. A., Rogers, R. F., Reasor, P. D., Uhlhorn, E. W., & Marks, F. D. (2013, October). Asymmetric hurricane boundary layer structure from dropsonde composites in relation to the environmental vertical wind shear. *Mon. Wea. Rev.*, *141*(11), 3968–3984. Retrieved from https://doi.org/10.1175/mwr-d-12-00335.1 doi: 10.1175/mwr-d-12-00335.1

Zhao, H., Yoshida, R., & Raga, G. B. (2015, July). Impact of the madden–julian oscillation on western north pacific tropical cyclogenesis associated with large-scale patterns. *J. App. Meteor. Clim.*, *54*(7), 1413–1429. Retrieved from https://doi.org/10.1175/jamc-d-14-0254.1 doi: 10.1175/jamc-d-14-0254.1

Zhou, W., Held, I. M., & Garner, S. T. (2014, February). Parameter study of tropical cyclones in rotating radiative–convective equilibrium with column physics and resolution of a 25-km GCM. *J. Atmos. Sci.*, *71*(3), 1058–1069. Retrieved from https://doi.org/10.1175/jas-d-13-0190.1 doi: 10.1175/jas-d-13-0190.1

Figure 1.

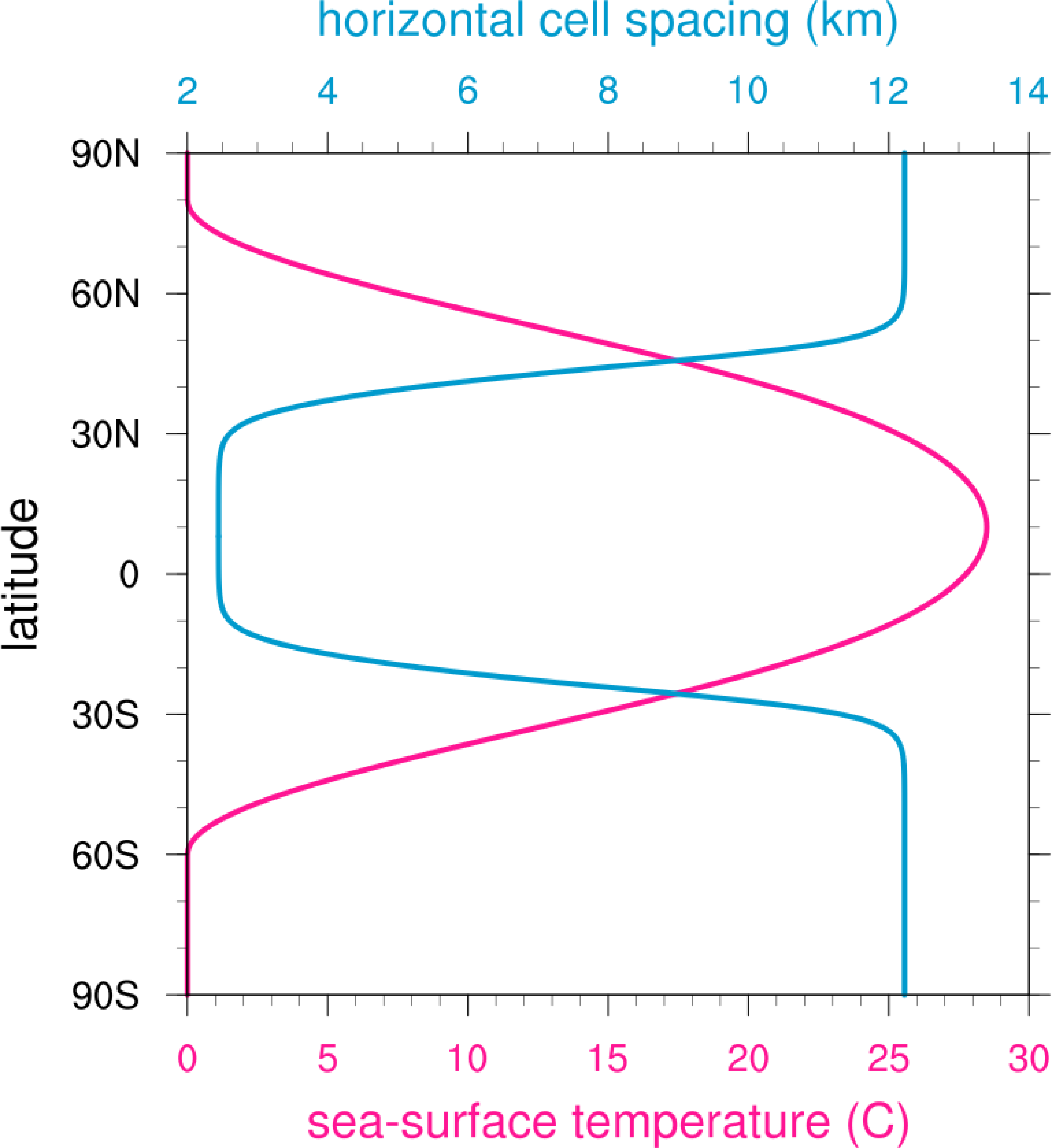
horizontal cell spacing (km)
2
4
6
8
10
12
14
90N
60N
30N
0
30S
60S
90S
latitude
0
5
10
15
20
25
30
sea-surface temperature (C)

Figure 2.

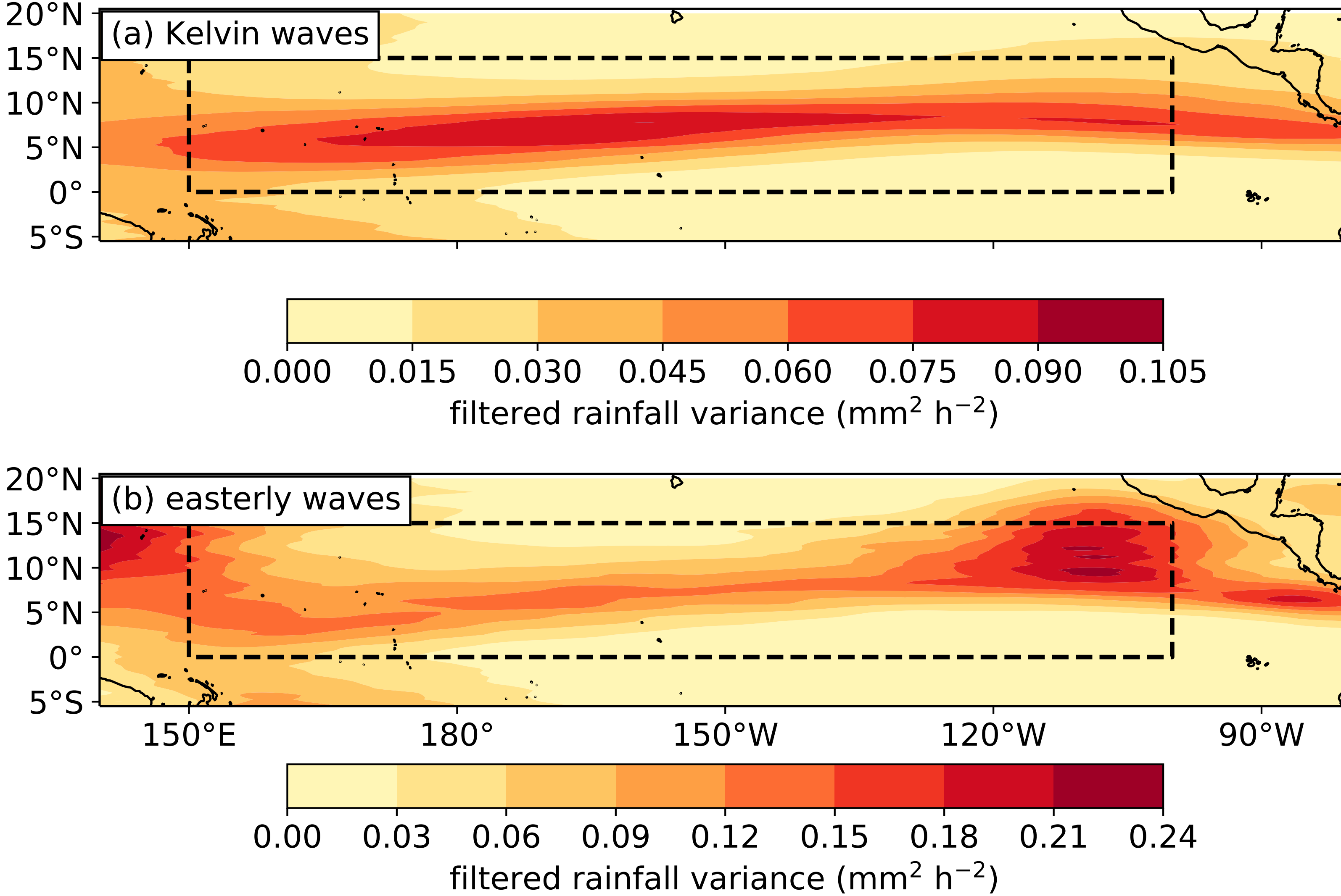

(a) Kelvin waves
20°N
15°N
10°N
5°N
0°
5°S
0.000
0.015
0.030
0.045
0.060
0.075
0.090
0.105
filtered rainfall variance ($mm^2\ h^{-2}$)
(b) easterly waves
20°N
15°N
10°N
5°N
0°
5°S
150°E
180°
150°W
120°W
90°W
0.00
0.03
0.06
0.09
0.12
0.15
0.18
0.21
0.24
filtered rainfall variance ($mm^2\ h^{-2}$)

Figure 3.

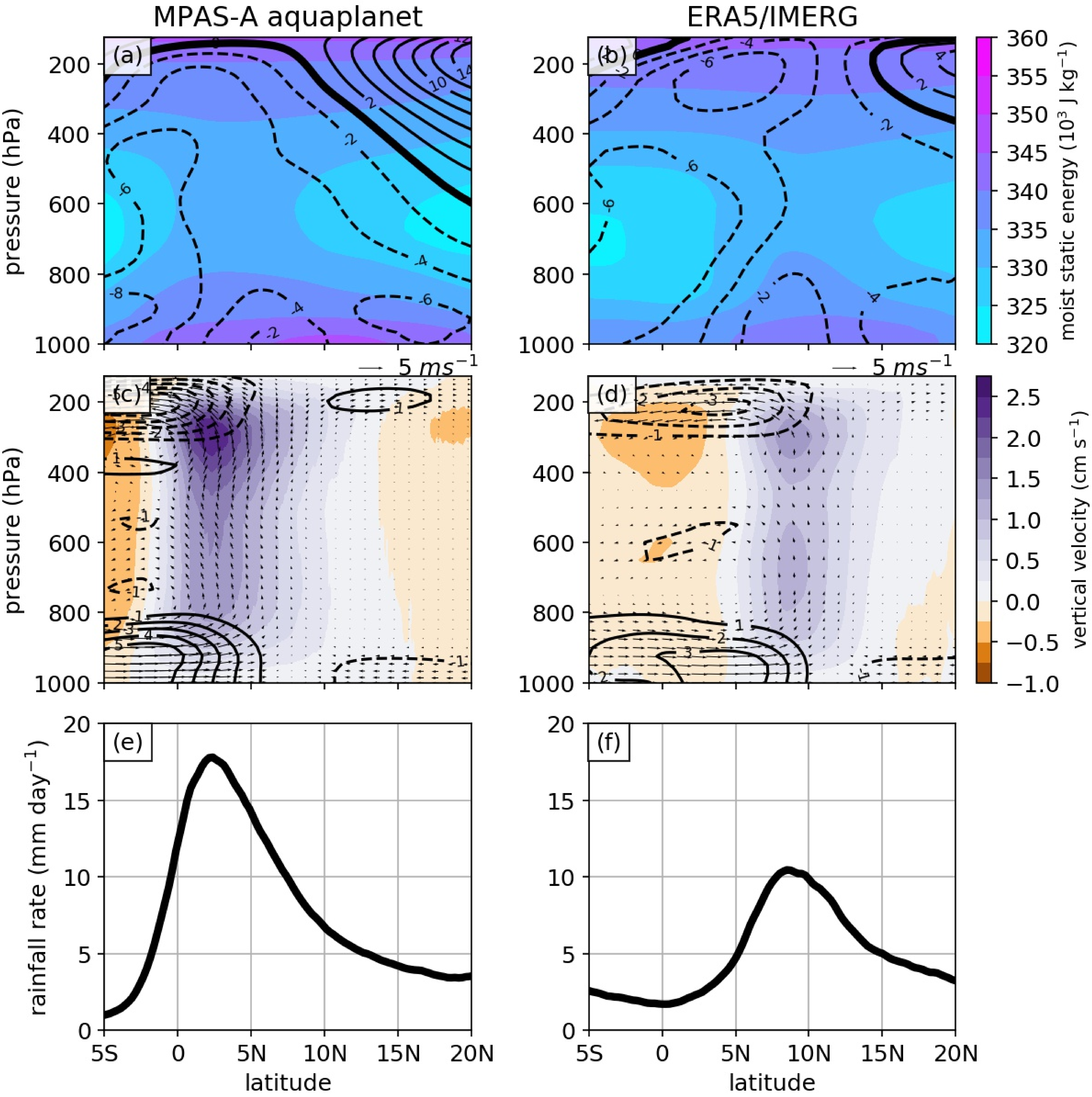

MPAS-A aquaplanet
ERA5/IMERG
(a)
(b)
(c)
(d)
(e)
(f)
pressure (hPa)
rainfall rate (mm day^{-1})
moist static energy (10^3 J kg^{-1})
vertical velocity (cm s^{-1})
5 ms^{-1}
latitude
5S
0
5N
10N
15N
20N

Figure 4.


80°N
60°N
40°N
20°N
0°
135°W
90°W
45°W
0°
45°E
90°E
135°E
LO
TS
H1
H2
H3
H4
H5
EX

Figure 5.

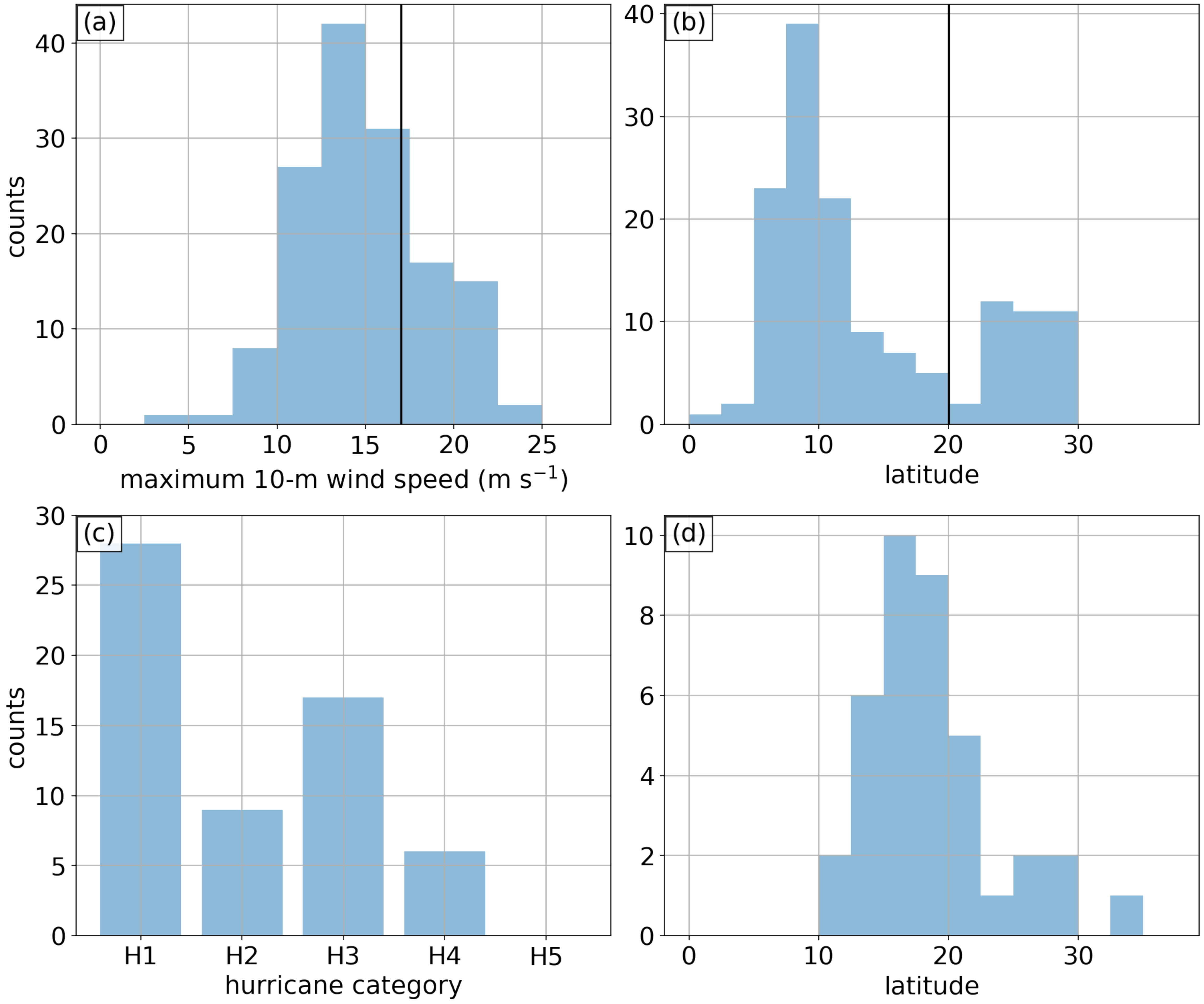
(a)
counts
maximum 10-m wind speed (m s^{-1})
(b)
latitude
(c)
counts
H1
H2
H3
H4
H5
hurricane category
(d)
latitude

Figure 6.

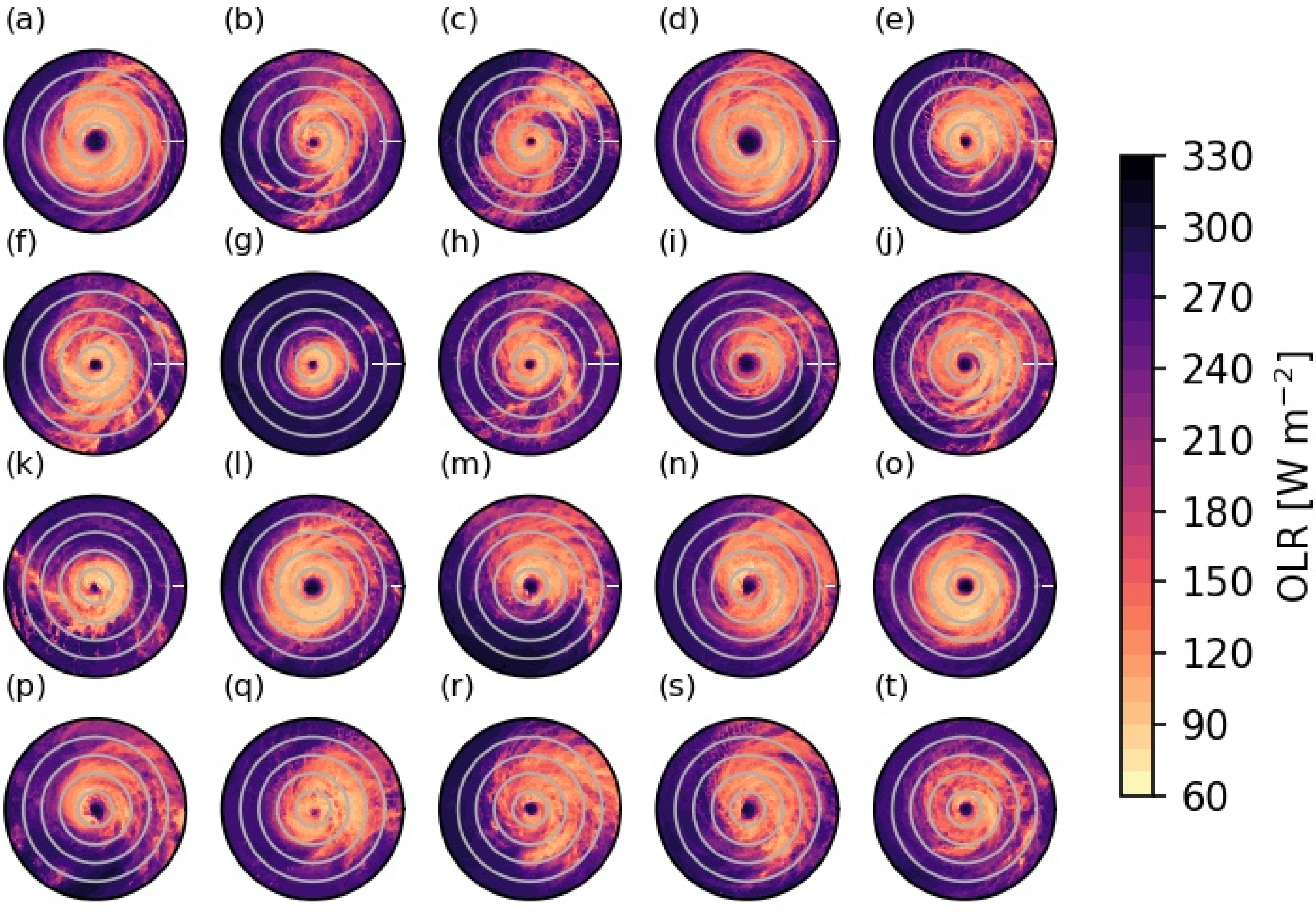
(a)
(b)
(c)
(d)
(e)
(f)
(g)
(h)
(i)
(j)
(k)
(l)
(m)
(n)
(o)
(p)
(q)
(r)
(s)
(t)
330
300
270
240
210
180
150
120
90
60
OLR [W m^{-2}]

Figure 7. composite_tanwind+radwind_MPAS+TC-DROPS.png

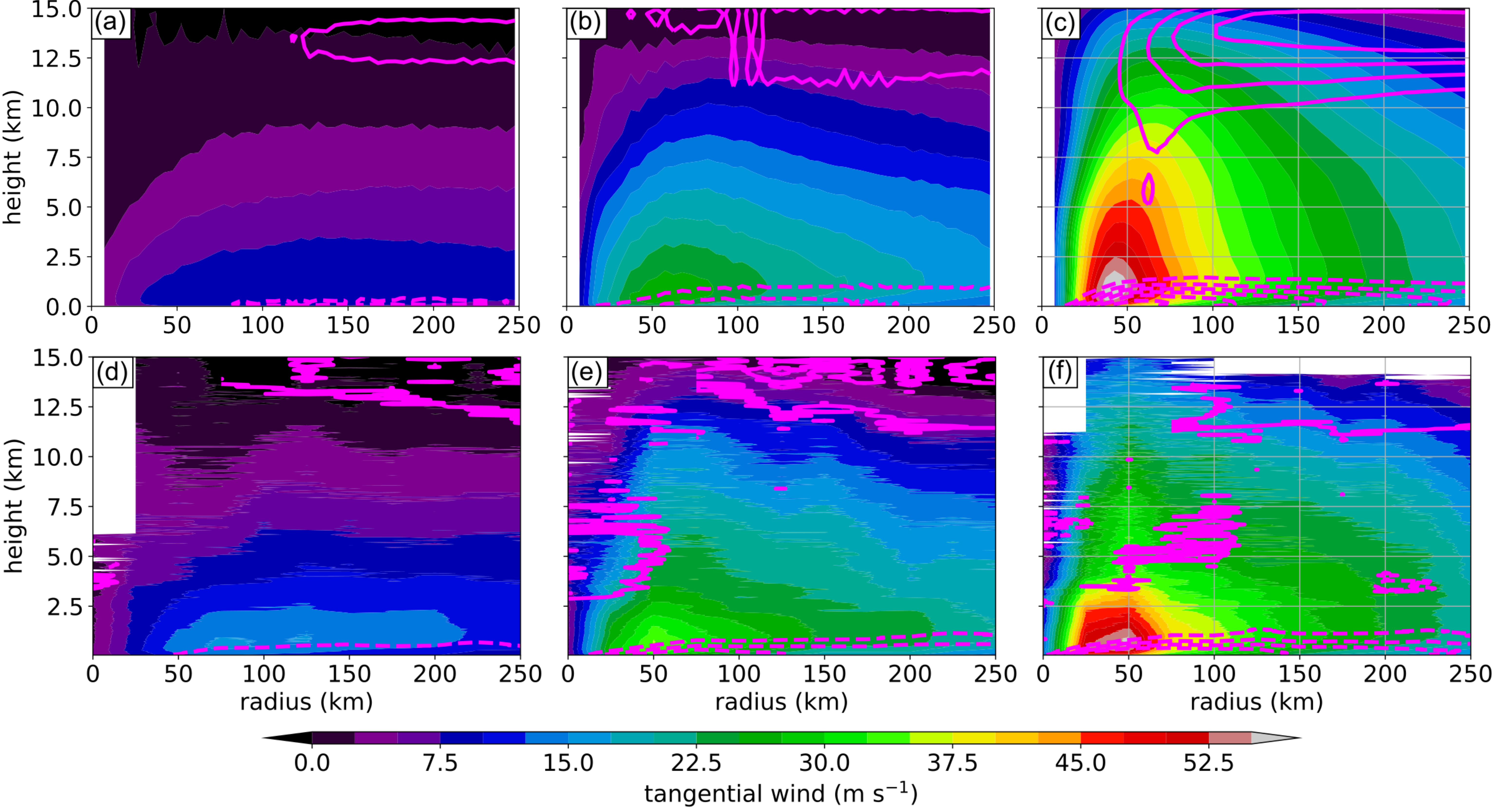

(a)
(b)
(c)
(d)
(e)
(f)
height (km)
radius (km)
0.0
2.5
5.0
7.5
10.0
12.5
15.0
0
50
100
150
200
250
0.0
7.5
15.0
22.5
30.0
37.5
45.0
52.5
tangential wind (m s^{-1})

Figure 8.

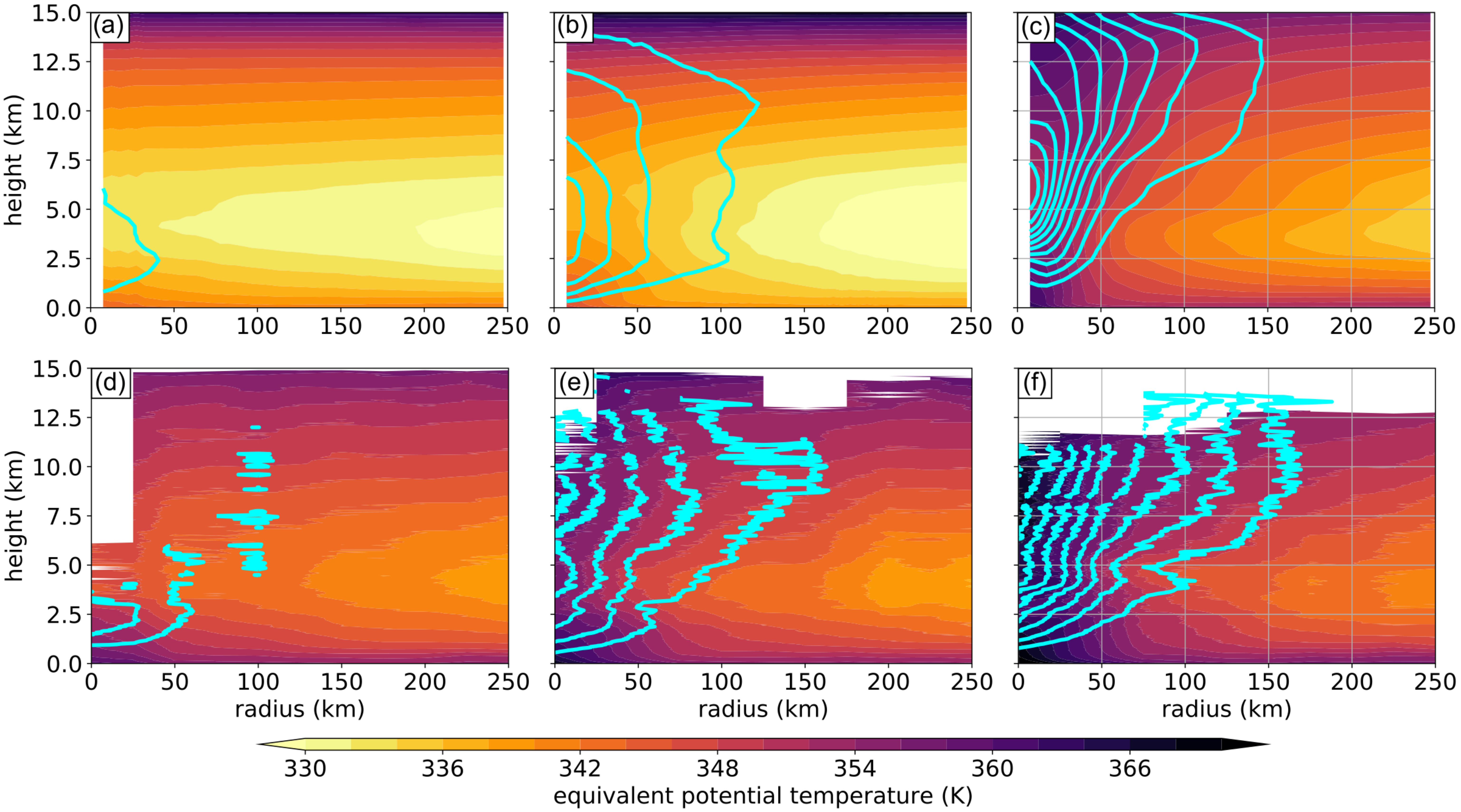

(a)
(b)
(c)
(d)
(e)
(f)
height (km)
radius (km)
15.0
12.5
10.0
7.5
5.0
2.5
0.0
0
50
100
150
200
250
330
336
342
348
354
360
366
equivalent potential temperature (K)

Figure 9.

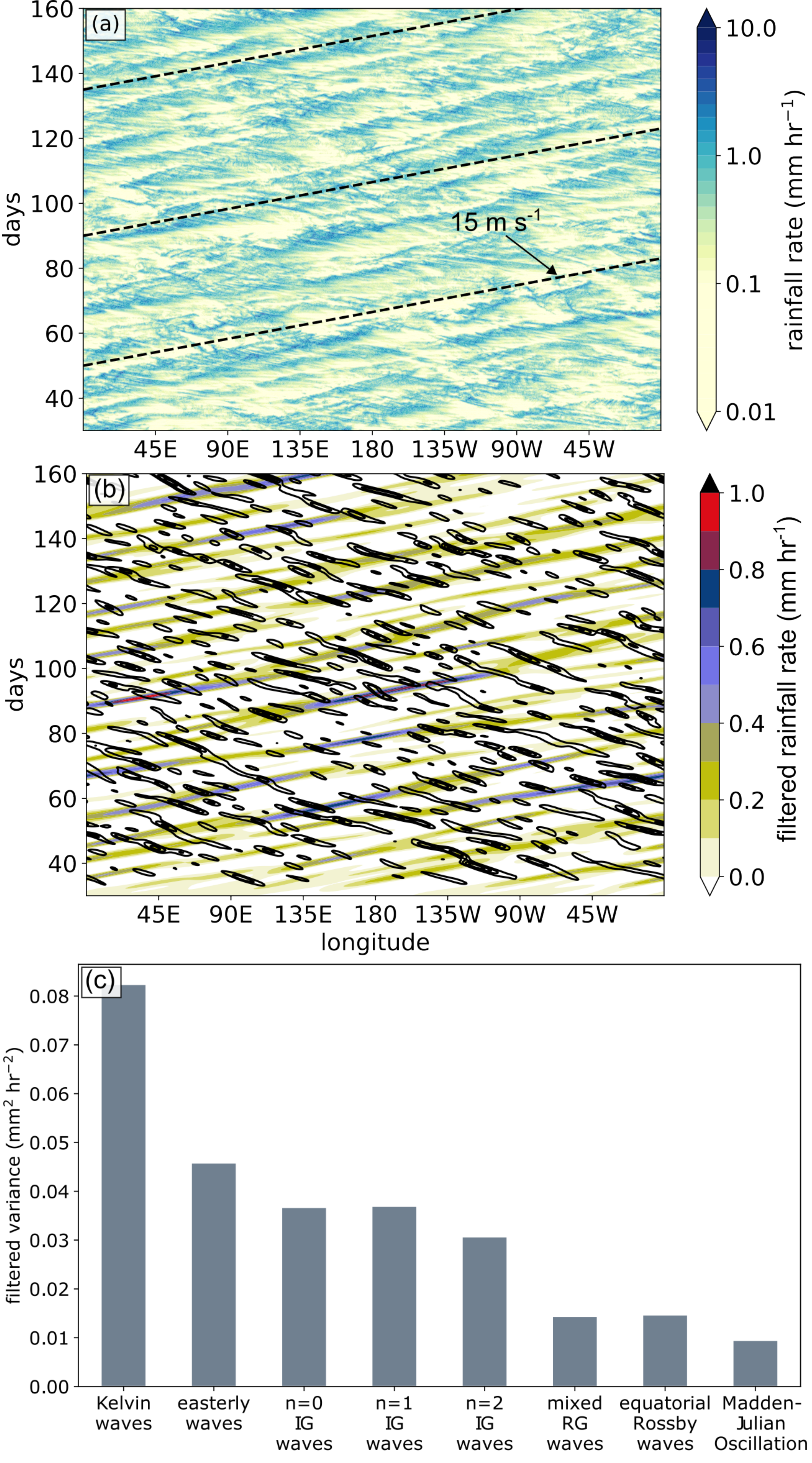

(a)
15 m s-1
days
rainfall rate (mm hr−1)
10.0
1.0
0.1
0.01
160
140
120
100
80
60
40
45E
90E
135E
180
135W
90W
45W
(b)
days
filtered rainfall rate (mm hr−1)
1.0
0.8
0.6
0.4
0.2
0.0
longitude
(c)
filtered variance (mm2 hr−2)
0.08
0.07
0.06
0.05
0.04
0.03
0.02
0.01
0.00
Kelvin waves
easterly waves
n=0 IG waves
n=1 IG waves
n=2 IG waves
mixed RG waves
equatorial Rossby waves
Madden-Julian Oscillation

Figure 10.

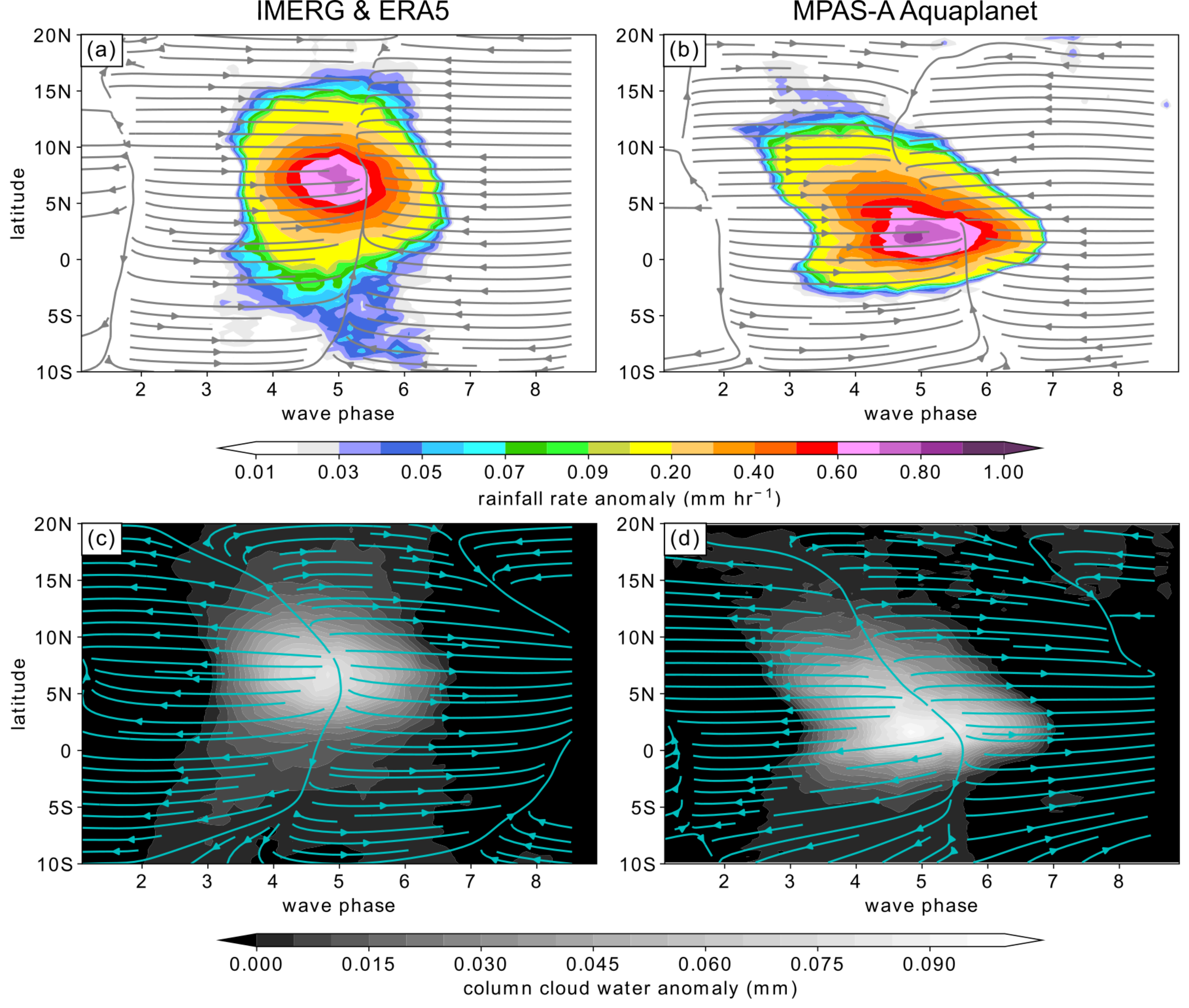
IMERG & ERA5
MPAS-A Aquaplanet
(a)
(b)
(c)
(d)
20N
15N
10N
5N
0
5S
10S
latitude
2
3
4
5
6
7
8
wave phase
0.01
0.03
0.05
0.07
0.09
0.20
0.40
0.60
0.80
1.00
rainfall rate anomaly (mm hr^{-1})
0.000
0.015
0.030
0.045
0.060
0.075
0.090
column cloud water anomaly (mm)

Figure 11.

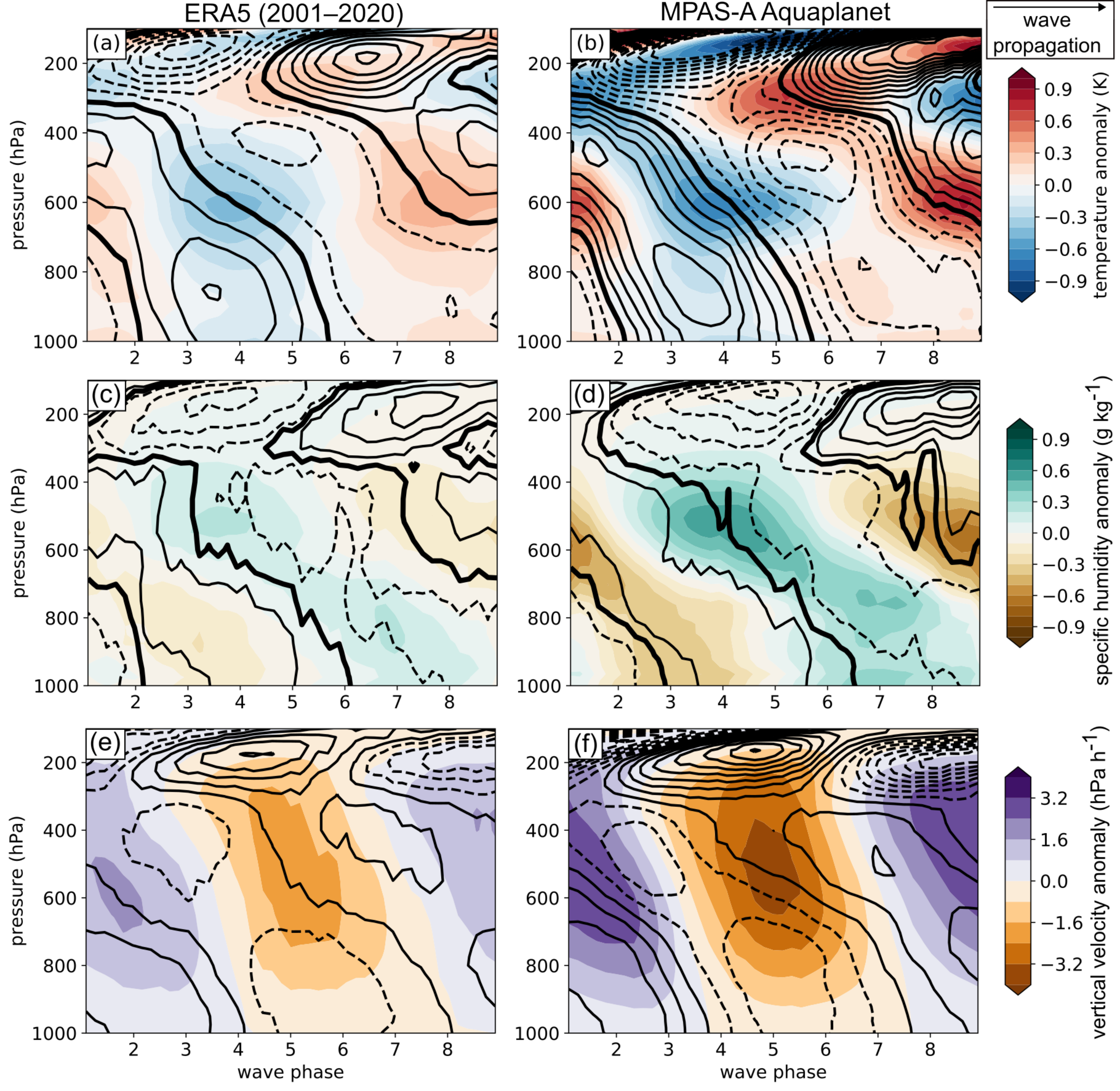
ERA5 (2001–2020)
MPAS-A Aquaplanet
wave propagation
(a)
(b)
(c)
(d)
(e)
(f)
pressure (hPa)
wave phase
temperature anomaly (K)
specific humidity anomaly (g kg^{-1})
vertical velocity anomaly (hPa h^{-1})

Figure 12.

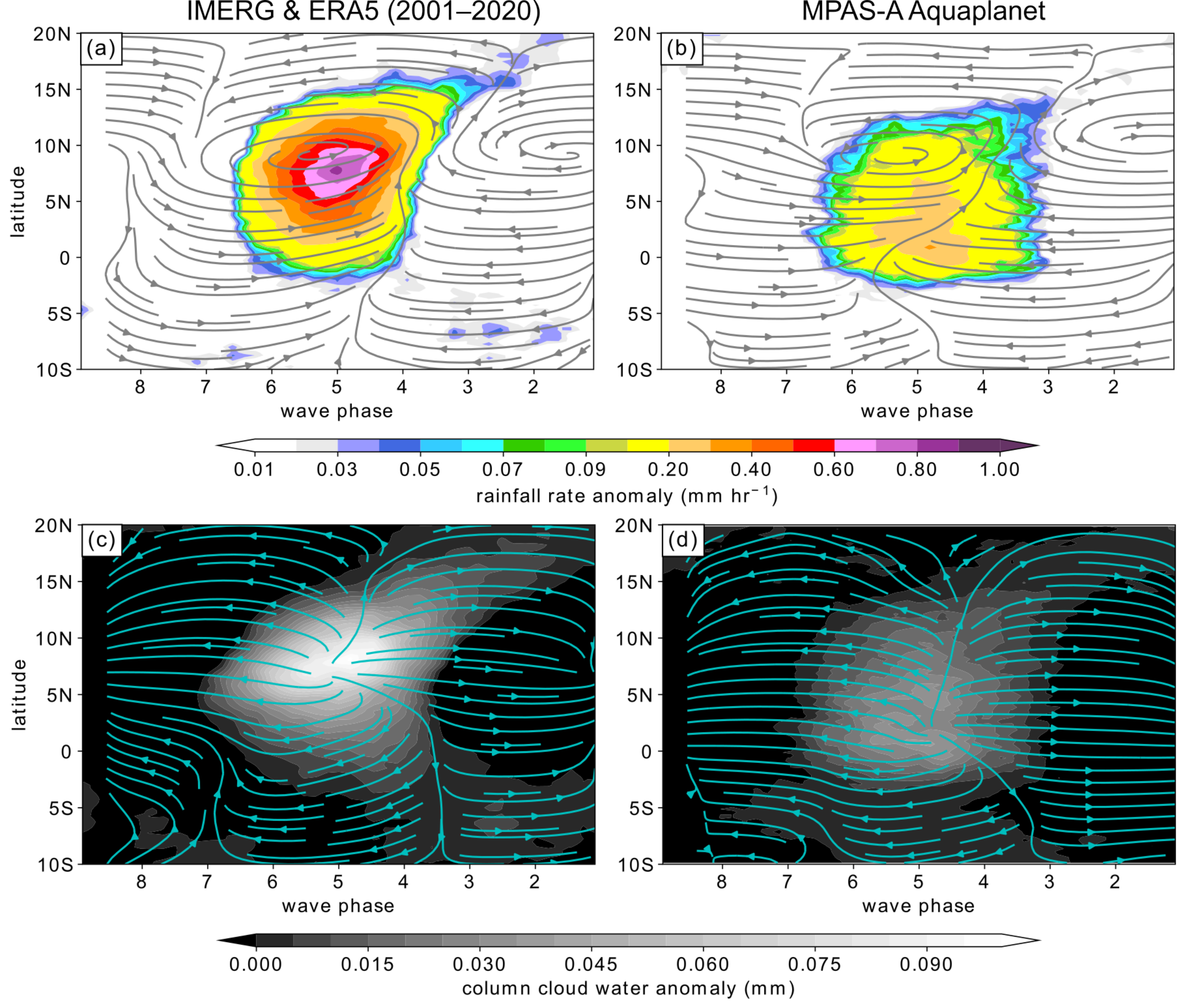

IMERG & ERA5 (2001–2020)
MPAS-A Aquaplanet
(a)
(b)
(c)
(d)
20N
15N
10N
5N
0
5S
10S
latitude
8
7
6
5
4
3
2
wave phase
0.01
0.03
0.05
0.07
0.09
0.20
0.40
0.60
0.80
1.00
rainfall rate anomaly (mm hr^{-1})
0.000
0.015
0.030
0.045
0.060
0.075
0.090
column cloud water anomaly (mm)

Figure 13.

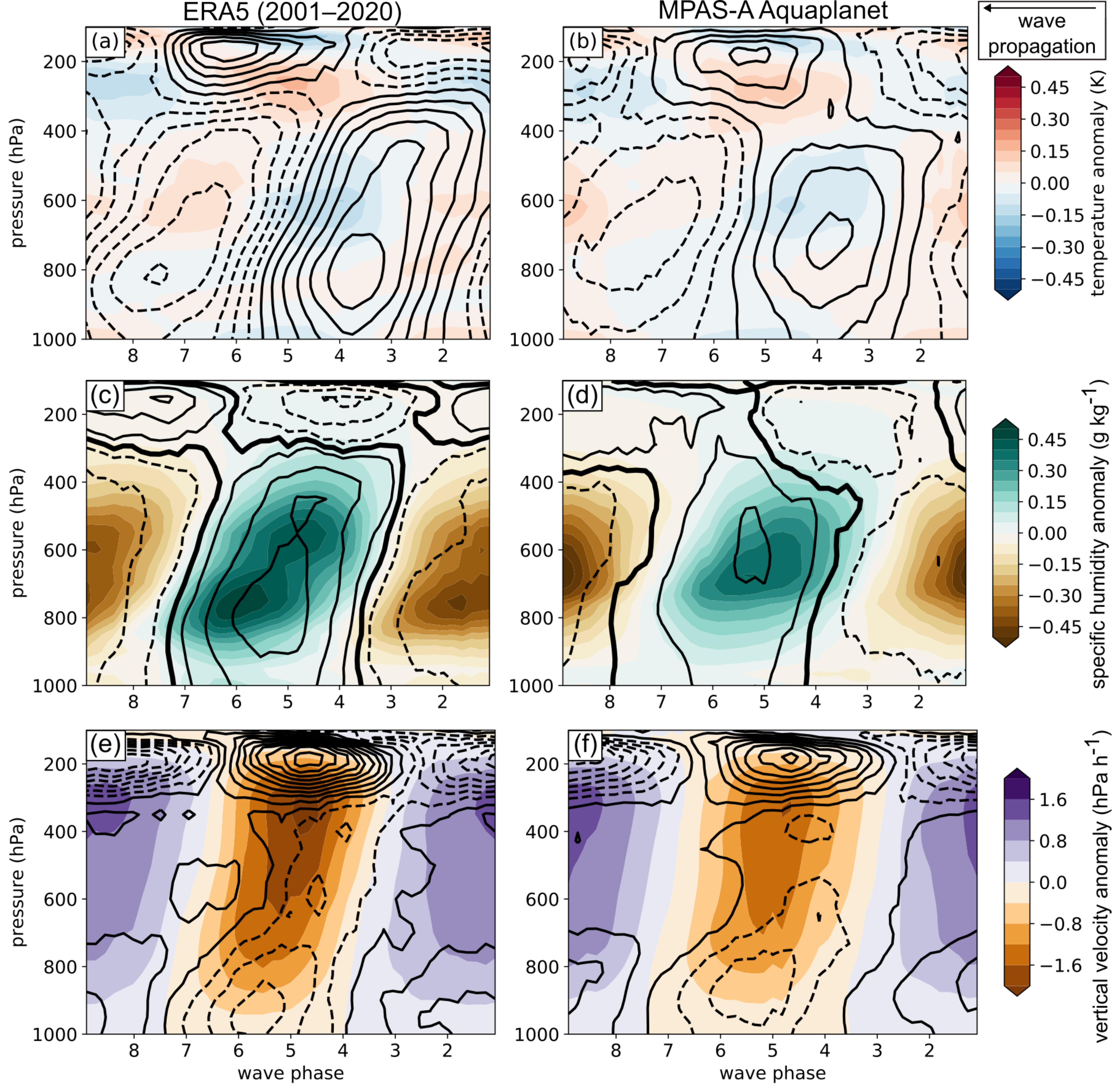

ERA5 (2001–2020)
MPAS-A Aquaplanet
wave propagation
(a)
(b)
(c)
(d)
(e)
(f)
pressure (hPa)
wave phase
temperature anomaly (K)
specific humidity anomaly (g kg^{-1})
vertical velocity anomaly (hPa h^{-1})